

Chapter 6

Electrodeposition of Rare Earth Metal in Ionic Liquids

Masahiko Matsumiya

Abstract It is very important to develop the recovery process of Nd and Dy metals using ionic liquids from a standpoint of establishing an environmental harmonization system and a recycling-oriented society. For this purpose, the solubility, the solvation structures, the electrochemical behaviors, the diffusive properties, the nucleation, and the electrodeposition behaviors were investigated for Nd(III) and Dy(III) in ionic liquids on this study.

As for the solvation analysis of Nd(III) and Dy(III) by Raman spectroscopy, the solvation numbers of Nd(III), Dy(II), and Dy(III) in [P₂₂₂₅][TFSA] were 5.1, 3.8, and 5.0, respectively. These results also revealed that the solvation structures of Nd(III), Dy(II), and Dy(III) were [Nd(TFSA)₅]²⁻, [Dy(TFSA)₄]²⁻, and [Dy(TFSA)₅]²⁻, respectively.

According to the electrochemical analyses with semi-integral and semi-differential methods, the reduction process of [Nd(TFSA)₅]²⁻ or [Dy(TFSA)₅]²⁻ proceeded in one step, [Nd(TFSA)₅]²⁻ + 3e⁻ → Nd(0) + 5[TFSA]⁻, or two steps, [Dy(TFSA)₅]²⁻ + e⁻ → [Dy(TFSA)₄]²⁻ + [TFSA]⁻ and [Dy(TFSA)₄]²⁻ + 2e⁻ → Dy(0) + 4[TFSA]⁻, respectively. The activation energies of the diffusion coefficients for [Nd(TFSA)₅]²⁻ and [Dy(TFSA)₅]²⁻ were 52.8 and 53.4 kJ mol⁻¹, respectively, and these behaviors were related to the similar solvation structures. The nucleation behaviors of [Nd(TFSA)₅]²⁻ and [Dy(TFSA)₅]²⁻ were altered from instantaneous to progressive nucleation by increasing the overpotential. The potentiostatic electrodepositions of Nd and Dy were also carried out and the recovered blackish electrodeposits were Nd and Dy metals evaluated by XPS. Finally, we demonstrated that the recovery process of Nd metal from spent Nd–Fe–B magnets by wet separation and electrodeposition using ionic liquids was effective.

Keywords Solubility of Nd(III) and Dy(III) in ionic liquids • Solvation structures of Nd(III) and Dy(III) in ionic liquids • Electrochemical behaviors of Nd(III) and Dy(III) in ionic liquids • Nucleation behaviors of Nd(III) and Dy(III) in ionic

M. Matsumiya (✉)

Graduate School of Environment and Information Sciences, Yokohama National University,
79-2 Tokiwadai, Hodogaya-ku, Yokohama 240-8501, Japan
e-mail: mmatsumi@ynu.ac.jp

liquids • Electrodeposition of Nd and Dy metals in ionic liquids • Recovery process of Nd metal from spent Nd–Fe–B magnets

6.1 Introduction

Rare earth (RE) elements have become essential for high-tech industry, where they have been applied to many technical fields such as optical materials [1, 2], laser materials [3], and magnetic materials [4] due to their original properties. The demand of RE metals and oxides has drastically increased in recent years. However, the import situation of RE compounds has been influenced by the supply restrictions of the main exporting countries [5]. In addition, the supply of RE related compounds is occasionally unstable in certain parts of the world, where it is currently difficult to supply such RE elements locally, and thus Japan has been largely dependent on other countries for the supply of RE compounds. As one of RE elements, Nd has been incorporated into Nd₂Fe₁₄B permanent magnets (Nd–Fe–B magnets) and Dy has also found similar application. Nd–Fe–B magnets are utilized in a variety of high technology products, e.g., voice coil motors (VCMs) for hard disk drives, magnetic field sources for magnetic resonance imaging (MRI), driving motors for hybrid-type electric vehicles, and so on [6]. The demand for Nd–Fe–B magnets has continued to elevate in recent years because these magnets play an important role in applications that require energy saving and efficiency. Hence, the recovery of Nd and Dy from the spent Nd–Fe–B magnets is necessary to secure a stable supply of these resources. Although the recovery process of Nd and Dy from spent Nd–Fe–B magnets has been actively studied [7–9], a practical recovery system has not been established to date. As one prospective means of recovering Nd and Dy metals, the electrodeposition using ionic liquids (ILs) is attractive from a standpoint of the environmental harmonization. The ILs have several attractive physicochemical properties, such as negligible vapor pressure, high ionic conductivity, and a wide electrochemical window [10, 11]. In particular, among the ILs consisting of bis(trifluoromethyl-sulfonyl) amide, [TFSA][−] has a good hydrophobicity.

There are a few reports about the electrodeposition of RE metals from the TFSA-based IL bath, e.g., La [12] in 1-octyl-1-methyl-pyrrolidinium bis(trifluoromethyl-sulfonyl)amide, [OMP][TFSA]; Eu [13] in *N,N,N*-trimethyl-*n*-butylammonium bis(trifluoromethyl-sulfonyl)amide, [N₁₁₁₄][TFSA]; and Dy [14] in dimethylformamide/dimethylpyrrolidinium trifluoromethanesulfonate (DMF/DMPT). Recently, we demonstrated the electrodeposition of Nd [15–19] and Dy [20, 21] from the TFSA-based IL bath, e.g., triethyl-pentyl-phosphonium bis(trifluoromethyl-sulfonyl)amide, [P₂₂₂₅][TFSA]; 2-hydroxyethyl-trimethyl-ammonium bis(trifluoromethyl-sulfonyl)amide, [N_{1112OH}][TFSA]; and *N,N*-diethyl-*N*-methyl-*N*-(2-methoxyethyl)ammonium bis(trifluoromethyl-sulfonyl)amide, [DEME][TFSA]. It is very important to electrodeposit Nd and Dy as a metallic state by elevating the bath temperature in order to decrease the overpotential of the electrodeposited metals. This elevation of the bath temperature is related to the important factors, e.g., the high solubility of RE amide

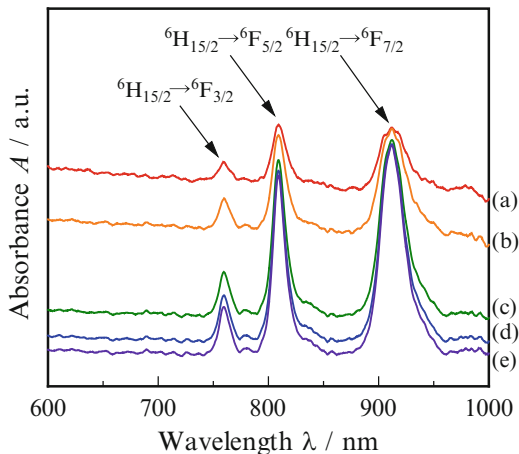
salts, high ionic conductivity, low viscosity of the ILs, and high diffusion coefficient of the RE complexes. The main results about the solubility, the solvation structure, the electrochemical behavior, the nucleation behavior, and the electrodeposition behavior are demonstrated in the following sections.

6.2 Solubility of Nd(III) and Dy(III)

The solubilities of Nd(TFSA)₃ and Dy(TFSA)₃ in [P₂₂₂₅][TFSA] neat solution were evaluated using an ultraviolet–visible (UV–Vis) spectroscopy spectrometer (ADC1000-USB, Ocean Optics Inc.) with a heating system. The UV–Vis measurement at elevated temperatures was required to investigate the temperature dependence of solubility for RE(TFSA)₃ salts. The heating system was composed of a spectrophotochemical thin-layer quartz microcell placed directly on the electrothermal equipment and covered with the ceramic fiber insulators (Kaowool Blanket, Aida Chemical Industries Co., Ltd.) in order to maintain the setting temperature of the measured samples. The temperature of the samples was measured using a K-type thermocouple ($\phi = 1.6$ mm) inserted into the quartz microcell (light path length: 1.0 cm) and was recorded by a data logger (midi logger GL220, Graphtec Co., Inc.). The accuracy of the temperature control in this system was ± 0.1 K. The wavelength regions of deuterium and halogen lamps for the UV–Vis were within the range of 180–870 and 340–1020 nm, respectively. For the evaluation for the solubility of RE(TFSA)₃ in ILs, the volume molality m (mol dm^{-3}) in the range of 1.0–3.0 mol dm^{-3} was applied to each sample using two types of solutes: Nd(TFSA)₃ and Dy(TFSA)₃ in [P₂₂₂₅][TFSA] solvent.

The accurate solubility measurement of RE(TFSA)₃ as a function of temperature is particularly essential for understanding the dissolution behavior in the IL media. In addition, it was more effective to prepare IL samples beforehand by dissolving Nd(TFSA)₃ or Dy(TFSA)₃ salts with constant volume molarity. For example, the variation of the absorption spectra of 1.0 mol dm^{-3} Dy(III) in [P₂₂₂₅][TFSA] undergoing a temperature increase is shown in Fig. 6.1. At room temperature, no absorption spectrum for Dy(III) could be observed because this IL sample turned opaque owing to partial solidification of a large amount of Dy(TFSA)₃ salt. As the operating temperature subsequently increased, three peaks began to appear at approximately 760 nm (${}^6\text{H}_{15/2} \rightarrow {}^6\text{F}_{5/2}$), 810 nm (${}^6\text{H}_{15/2} \rightarrow {}^6\text{F}_{5/2}$), and 911 nm (${}^6\text{H}_{15/2} \rightarrow {}^6\text{F}_{7/2}$), as shown in Fig. 6.1a. This spectroscopic behavior suggests that the IL dissolves the Dy(TFSA)₃ salt; therefore, the IL is altered from a semitransparent to a transparent state by increasing the temperature. The hypersensitive peak of Dy(III) appeared at 1290 nm (${}^6\text{H}_{15/2} \rightarrow {}^6\text{F}_{11/2}$) and the observed peak at 911 nm for ${}^6\text{H}_{15/2} \rightarrow {}^6\text{F}_{7/2}$ had a secondary intensity when compared to the hypersensitive peak. Thus, the ${}^6\text{H}_{15/2} \rightarrow {}^6\text{F}_{7/2}$ peak with the secondary intensity is a good evaluator of the Dy(III) solubility state. As the temperature increased further, the peak intensity for ${}^6\text{H}_{15/2} \rightarrow {}^6\text{F}_{7/2}$ also increased gradually. When the temperature reached 336 K, the spectrum of Dy(III) indicated maximum absorbance. Moreover, there

Fig. 6.1 The temperature dependence of the absorption spectrum of 1.0 mol dm^{-3} Dy(III) in $[\text{P}_{2225}][\text{TFSA}]$. (a) 323 K, (b) 333 K, (c) 335 K, (d) 336 K, (e) above 338 K



was no further alternation on the Dy(III) spectrum above 338 K (Fig. 6.1e). Therefore, the sample was completely dissolved at 336 K and the volume molarity of 0.1 mol dm^{-3} Dy(III) is saturated at this temperature. The similar measurements for all prepared samples were performed and the temperature of each sample that reached the saturation point was recorded. For Nd(III) in ILs, the solubility was evaluated from the hypersensitive peak (${}^4\text{I}_{9/2} \rightarrow {}^2\text{G}_{7/2}$) at 580 nm.

A series of experimental results on the volume molarity for Nd(III) and Dy(III) is shown in Fig. 6.2. These results reveal that the solubility curves of Nd(III) and Dy(III) tend toward a nonlinear relationship. The temperature dependence of the mole fraction solubility of Nd(III) and Dy(III) was fitted using the modified Apelblat equation [22, 23]:

$$\ln x^{\text{sol}} = A + \frac{B}{\tau} + \frac{C}{\tau^2} + \frac{D}{\tau^3} + E \ln \tau \quad (6.1)$$

where x^{sol} is the solubility of the solute in mole fraction; τ is equivalent to T/T_0 , where the scaling temperature is $T_0 = 405.65 \text{ K}$, which is the average empirical temperature for the solubility measurements and T is the absolute temperature; A , B , C , D , and E are the empirical parameters; and r^2 is the coefficient of determination as listed in Table 6.1. The logarithm of the mole fraction solubility, x^{sol} of Nd(III) and Dy(III) as a function of the inverse of the temperature, and the theoretical curves fitted by Eq. (6.1) are shown in Fig. 6.3.

The temperature dependence of the solubility curves of Nd(III) and Dy(III) displayed an analogous tendency. Free energy evaluation is the most reliable theoretical method for systematic studies of solvation properties [24, 25]. The thermodynamic properties characterizing the solvating process of the IL were derived from the temperature dependence of the solubility using Eq. (6.1):

Fig. 6.2 The temperature dependence of the solubility curve for Nd(III) and Dy(III) in [P₂₂₂₅][TFSA]. The error bar was evaluated from the temperature deviation. ○: Nd(III) and ●: Dy(III) (Reprinted with permission from Ref. [21] Copyright 2013, Elsevier Science)

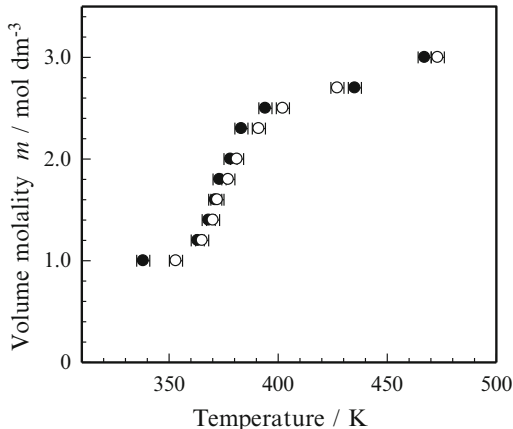
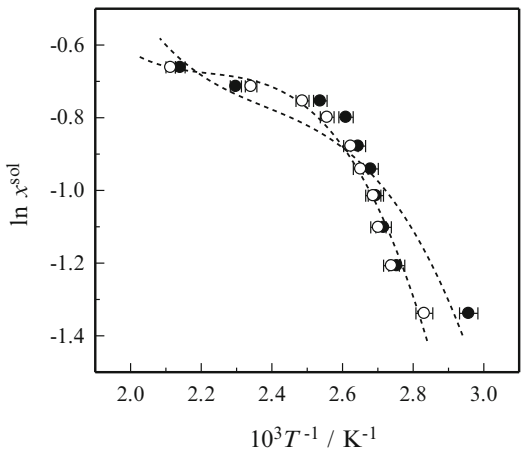


Table 6.1 The correlated parameters used to fit the experimental results in the modified Apelblat equation and the coefficient of determination

| | A | B | C | D | E | r ² |
|---------|---------|--------|--------|---------|--------|----------------|
| Nd(III) | -66.840 | 59.520 | 29.141 | -22.568 | 51.665 | 0.970 |
| Dy(III) | -63.178 | 55.183 | 25.713 | -18.523 | 52.146 | 0.841 |

Fig. 6.3 Arrhenius plots for the molar fraction solubility x of Nd(III) and Dy(III) in [P₂₂₂₅][TFSA] and the theoretical curves by modified Apelblat equation. ○: Nd(III) and ●: Dy(III) (Reprinted with permission from Ref. [21] Copyright 2013, Elsevier Science)



$$\Delta_{\text{sol}}G^\infty = -RT \ln x^{\text{sol}} = -RT \left(A + \frac{B}{\tau} + \frac{C}{\tau^2} + \frac{D}{\tau^3} + E \ln \tau \right) \quad (6.2)$$

$$\Delta_{\text{sol}}H^\infty = RT^2 \frac{\partial \ln x^{\text{sol}}}{\partial T} = -RT \left(\frac{B}{\tau} + \frac{2C}{\tau^2} + \frac{3D}{\tau^3} - E \right) \quad (6.3)$$

Fig. 6.4 Thermodynamic quantities of Nd(III) in [P₂₂₂₅][TFSA] estimated from temperature dependence of the solubility

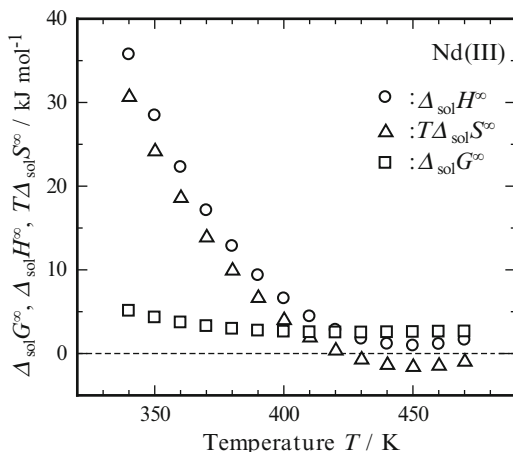
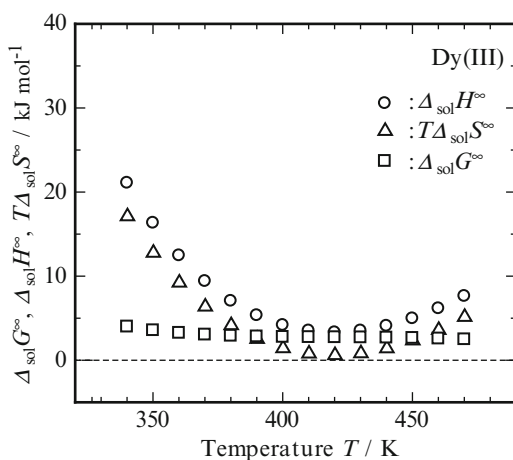


Fig. 6.5 Thermodynamic quantities of Dy(III) in [P₂₂₂₅][TFSA] estimated from temperature dependence of the solubility



$$\Delta_{\text{sol}}S^\infty = \frac{\Delta_{\text{sol}}H^\infty - \Delta_{\text{sol}}G^\infty}{T} = R \left(A - \frac{C}{\tau^2} - \frac{2D}{\tau^3} + E \ln \tau + E \right) \quad (6.4)$$

The calculated thermodynamic quantities of Nd(III) and Dy(III) with temperature dependence are shown in Figs. 6.4 and 6.5, respectively. The values of $\Delta_{\text{sol}}G^\infty$ regarding the interaction between the RE(TFSA)₃ salts and the IL solvent appeared to be reasonable, because the polar IL solvent exhibits positive values. The dissolution of RE(TFSA)₃ salts in ILs is enthalpy controlled. The values of $\Delta_{\text{sol}}H^\infty$ roughly followed those of $\Delta_{\text{sol}}G^\infty$ above 420 K, and entropy alternations for the dissolution process were close to zero. Assuming the small volume terms are ignored, the solvation free energy is equivalent to the interaction energy and is explained from the summation of the electrostatic interaction energy and the van der Waals interaction energy between the solute and solvent molecules [25]. For

this polar IL solvent, the van der Waals interaction would be weakened by the increase in the solvation energy. Concerning with the solubility evaluation of a solid solute into a polar IL solvent, there is a report on the dissolution of the elemental sulfur in the nonpolar toluene and polar imidazolium-based IL mixtures [23]. As for the dissolution of sulfur, the van der Waals interaction was weakened by the addition of polar imidazolium-based IL in the nonpolar toluene. This dissolution behavior was consistent with our results. The solubility curves are also important indicators of the applicability of electrodeposition in retrieving RE metals from phosphonium-based ILs.

6.3 Solvation Analysis of Nd(III) and Dy(III)

6.3.1 Solvation Structure of Nd(III)

Raman spectra of $[P_{2225}][TFSA]$ containing 0.2, 0.3, 0.4, and 0.5 mol dm⁻³ Nd (TFSA)₃ were investigated in this study. The water contents of all samples were confirmed to be less than 100 ppm. Raman spectra were measured at a temperature of 298 and 423 K using a 532 or 785 nm laser of Raman spectrometer (Renishaw inVia Reflex Raman Microscope). Spectral data were accumulated 512 times in order to obtain data of a sufficiently high S/N ratio. The free $[TFSA]^-$ anions had a characteristic intense band at 744 cm⁻¹, which was ascribed to the CF₃ bending vibration, $\delta_s(CF_3)$ coupled with the S-N stretching vibration $\nu_s(S-N-S)$ [26, 27]. In addition, there was an intense band at 750 cm⁻¹, which was ascribed to the $[TFSA]^-$ anions surrounding for the Nd(III). As the concentration of Nd(III) increased, the intensity positioned at 744 cm⁻¹ decreased. On the other hand, as the concentration of Nd(III) in $[P_{2225}][TFSA]$ increased, the intensity assigned at 750 cm⁻¹ increased. The obtained Raman spectra were deconvoluted to extract single Raman band for each assignment as shown in Fig. 6.6. A single Raman band was assumed to be represented as a pseudo-Voigt function, which consisted of the Lorentzian and Gaussian components. Moreover, based on Eq. (6.5) suggested in the reference [28], the solvation number of Nd(III) was analyzed from the following equation:

$$I_f/c_M = J_f(c_T/c_M - n) \quad (6.5)$$

where I_f is integral intensity, c_M is the concentration of Nd(III) in $[P_{2225}][TFSA]$, J_f is the molar Raman scattering coefficient, c_T is the total concentration of $[TFSA]^-$ anion, and n is the solvation number.

The integrated intensity of the deconvoluted Raman band of the free $[TFSA]^-$ in the bulk IL is represented as $I_f = J_f c_f$. The c_f is given as $c_f = c_T - c_b = c_T - n c_M$, which c_T and c_b denote the concentrations of total and bound $[TFSA]^-$ (solvated to the metal ion), respectively. The relationship between I_f/c_{Nd} and c_T/c_{Nd} is shown in

Fig. 6.6 The deconvoluted Raman spectra of [P₂₂₂₅][TFSA] including (a) 0.3, (b) 0.4, (c) 0.5, and (d) 0.6 mol dm⁻³ Nd(TFSA)₃.

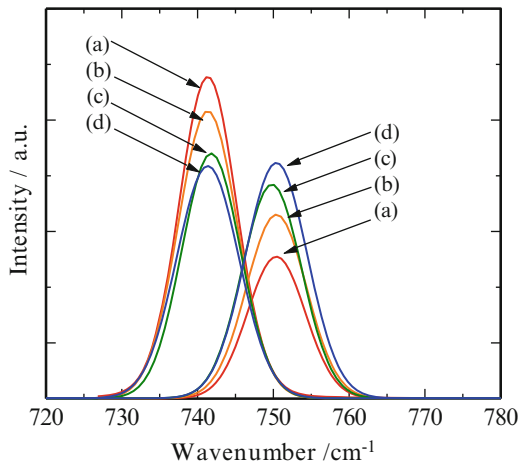


Fig. 6.7 The plot between I_f/c_{Nd} plots and R for Nd(III) in [P₂₂₂₅][TFSA]

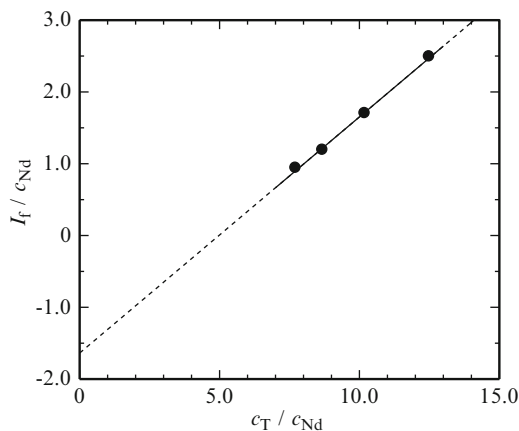


Fig. 6.7 and resulted in a straight line. Thus, the solvation number, n , is obtained as $n = \beta/\alpha$ from a slope $\alpha = J_f$ and an intercept $\beta = -J_f n$. In this study, the solvation number of Nd(III) in [P₂₂₂₅][TFSA] was calculated to be 5.1. The solvation structure between [Nd³⁺] cation and [TFSA]⁻ anion was indicated as a complexation of [Nd(TFSA)₅]²⁻.

6.3.2 Solvation Structure of Dy(III)

The deconvoluted Raman spectra with the concentration dependence in the frequency range 720–780 cm⁻¹ for 0.23–0.45 mol kg⁻¹ Dy(III) in [P₂₂₂₅][TFSA] were separated into two components at approximately 740 and 749 cm⁻¹, as shown in

Fig. 6.8 The deconvoluted Raman spectrum of Dy(III) in $[P_{2225}][TFSA]$ with the concentration dependence, (a) 0.23 mol kg^{-1} , (b) 0.30 mol kg^{-1} , (c) 0.38 mol kg^{-1} , and (d) 0.45 mol kg^{-1} Dy(III) (Reprinted with permission from Ref. [21] Copyright 2013, Elsevier Science)

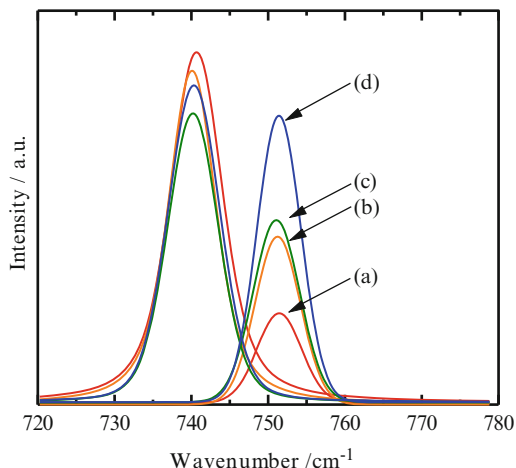


Fig. 6.9 Relationship between c_T/c_{Dy} and I_f/c_{Dy} for $[P_{2225}][TFSA]$ including Dy(II)/Dy(III) coexisted sample or Dy(III), \circ : Dy(II)/Dy(III) coexisted sample and \bullet : Dy(III) (Reprinted with permission from Ref. [21] Copyright 2013, Elsevier Science)

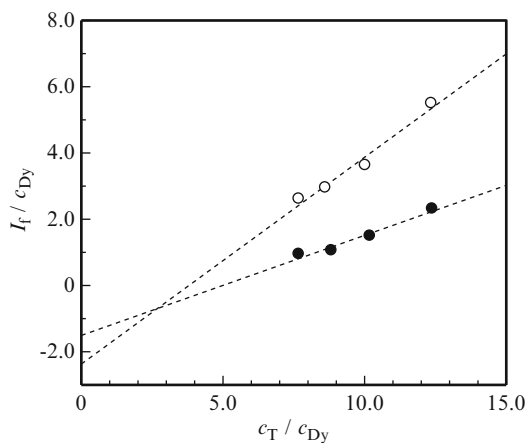


Fig. 6.8. As shown in this figure, a new band was observed as a shoulder on the high frequency side (747 cm^{-1}) of the intense band (740 cm^{-1}); this new band was intensified by increasing the Dy(III) concentration. Therefore, the band at 747 cm^{-1} in the present system is also considered to be due to the $[TFSA]^-$ anion bound to the Dy(III), and the vibrational mode of the band at 740 cm^{-1} corresponds to that of the free $[TFSA]^-$ anion.

The number of $[TFSA]^-$ anion solvated to the Dy(III) can be evaluated from the plots of I_f/c_M vs. c_T/c_M , as shown in Fig. 6.9. This plot demonstrates a strong linear relationship with an estimated n value of 5.0. This result suggests that $[Dy^{3+}]$ in $[P_{2225}][TFSA]$ is solvated by five $[TFSA]^-$ anions and $[Dy(TFSA)_5]^{2-}$ complexation occurred in this system. The Raman spectrum of the Dy(II)/Dy(III) mixed sample also highlights the concentration dependence of the Dy(II)/Dy(III) ratio in the frequency range $720\text{--}780 \text{ cm}^{-1}$. A similar analysis of the solvent number was

performed on the deconvoluted data, and the obtained solvation number was 3.8, as shown in Fig. 6.9. This result suggests that the Dy(II) exists in this IL system and the solvation structure: $[\text{Dy}(\text{TFSA})_4]^{2-}$ would be smaller than $[\text{Dy}(\text{TFSA})_5]^{2-}$.

As for the fluorescence spectroscopy, an energy diagram reported for Dy(III) [29, 30] has indicated that the fluorescence emission of $[\text{Dy}(\text{TFSA})_5]^{2-}$ is mainly due to the radiative transitions from the excited ${}^4\text{F}_{9/2}$ and ${}^4\text{I}_{13/2}$ to the ground multiplet of ${}^6\text{H}_{J/2}$ ($J=7-15$). The fluorescence spectra of $[\text{Dy}(\text{TFSA})_5]^{2-}$ and the equimolar $[\text{Dy}(\text{TFSA})_4]^{2-}/[\text{Dy}(\text{TFSA})_5]^{2-}$ samples were also investigated in this study. The yellow-colored emission at 572 nm (due to the hypersensitive transition of ${}^4\text{F}_{9/2} \rightarrow {}^6\text{H}_{13/2}$) and the blue-colored emission at 479 nm (due to the ${}^4\text{F}_{9/2} \rightarrow {}^6\text{H}_{15/2}$ transition) [31, 32] were noticeably observed in the $[\text{Dy}(\text{TFSA})_5]^{2-}$ samples. However, the normalized fluorescence intensity of the equimolar $[\text{Dy}(\text{TFSA})_4]^{2-}/[\text{Dy}(\text{TFSA})_5]^{2-}$ sample at 572 nm was drastically smaller than that of the $[\text{Dy}(\text{TFSA})_5]^{2-}$ sample. This result suggests that the Dy(III) is reduced to the Dy(II), which is consistent with the above Raman investigation.

6.4 Physicochemical Properties of Nd(III)

The temperature dependence of the viscosity and the ionic conductivity for 0.5 mol dm^{-3} $[\text{Nd}(\text{TFSA})_5]^{2-}$ in $[\text{P}_{2225}][\text{TFSA}]$ with various water contents was expressed in Figs. 6.10 and 6.11, respectively. The data for $[\text{P}_{2225}][\text{TFSA}]$ neat solution was also plotted in each figure.

In comparison with the $[\text{P}_{2225}][\text{TFSA}]$ neat solution, the viscosity of the $[\text{P}_{2225}][\text{TFSA}]$ including $[\text{Nd}(\text{TFSA})_5]^{2-}$ increased in the whole temperature range. It was also observed that the ionic conductivity of this $[\text{P}_{2225}][\text{TFSA}]$ dissolving $[\text{Nd}(\text{TFSA})_5]^{2-}$ decreased in the same temperature range. Thus, it was revealed that $[\text{Nd}(\text{TFSA})_5]^{2-}$ complex was influenced by the transport property and the

Fig. 6.10 Viscosity of $[\text{P}_{2225}][\text{TFSA}]$ and 0.5 mol dm^{-3} $[\text{Nd}(\text{TFSA})_5]^{2-}$ in $[\text{P}_{2225}][\text{TFSA}]$ at different water contents

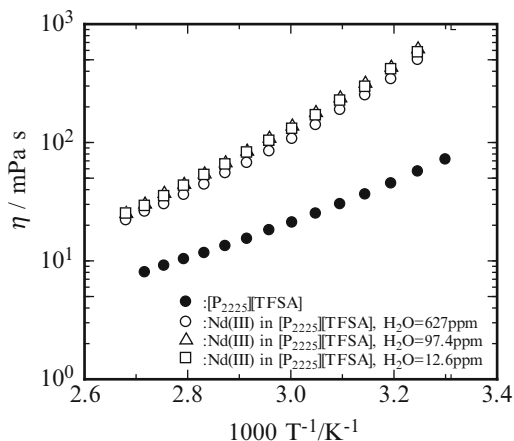


Fig. 6.11 Ionic conductivity of $[P_{2225}][TFSA]$ and $0.5 \text{ mol dm}^{-3} [Nd(TFSA)_5]^{2-}$ in $[P_{2225}][TFSA]$ at different water contents

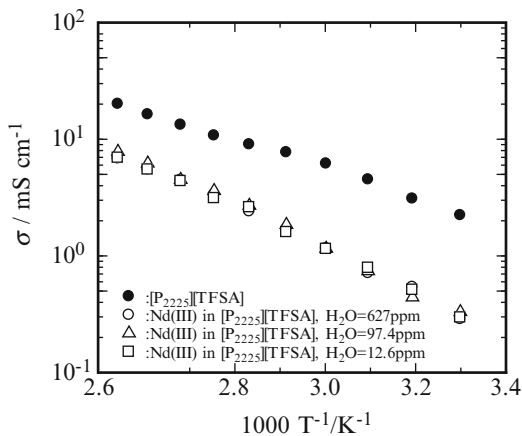
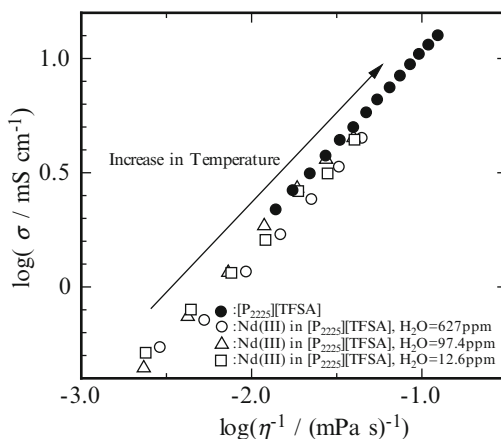


Fig. 6.12 Plots of the ionic conductivity against the inverse of the viscosity for $[P_{2225}][TFSA]$ and $0.5 \text{ mol dm}^{-3} [Nd(TFSA)_5]^{2-}$ in $[P_{2225}][TFSA]$ with different water contents based on Walden rule



conductive carrier. On the other hand, the viscosity decreased and the ionic conductivity increased by elevating the temperature. The trend of the viscosity and the ionic conductivity of $[N_{1116}][TFSA]$ containing various metallic amide salts indicated the similar tendency in the case of applying some kinds of metallic salts such as transition and RE elements [33]. In addition, these physicochemical properties were not severely influenced by the water content when it is less than 100 ppm in the electrolyte. Eventually, this result demonstrated that the ionic conduction of the IL was mainly caused by the transportation of metallic complexes and ions.

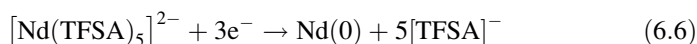
The ionic conductivity against the inverse viscosity based on Walden rule [34] is shown in Fig. 6.12. The relationship between these physicochemical properties under the same condition in log–log scale displayed clearly a straight line. This result also indicated that a kind of Walden rule ($\sigma\eta = \text{constant}$) was applicable for $[P_{2225}][TFSA]$ including $[Nd(TFSA)_5]^{2-}$ with and without trace amounts of water.

This linear relation was revealed that both the ionic species and metallic species in the bulk electrolyte were associated with each other and the mass transfer of the metallic species contributed to the ionic conductivity. The mass transfer of the metallic species was also correlated with the ionic mobility. In the case of electro-deposition from this kind of $[P_{2225}][TFSA]$ including $[Nd(TFSA)_5]^{2-}$, the mobility of metallic ions and related complexes would be influenced by the current efficiency of the cathodic process.

6.5 Electrochemical Behaviors of Nd(III) and Dy(III)

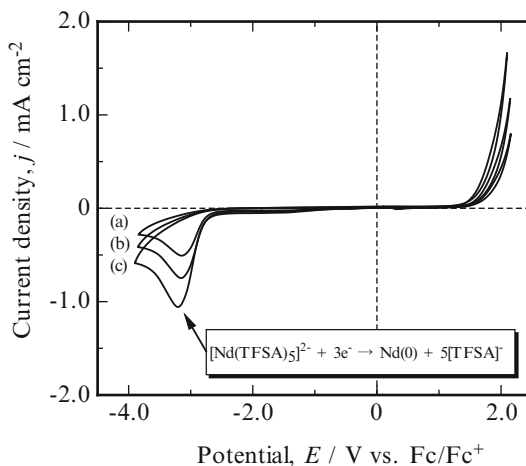
6.5.1 Electrochemical Behavior of Nd(III)

The reduction behavior of $[Nd(TFSA)_5]^{2-}$ in $[P_{2225}][TFSA]$ was investigated by CV. The cyclic voltammogram of $0.5 \text{ mol dm}^{-3} [Nd(TFSA)_5]^{2-}$ in $[P_{2225}][TFSA]$ using a Pt electrode at 353 K is shown in Fig. 6.13. This cyclic voltammogram was scanned cathodically from the initial potential of 0.0 V. A cathodic peak was observed around -3.30 V . The electrodeposits obtained from $[Nd(TFSA)_5]^{2-}$ in $[P_{2225}][TFSA]$ by potentiostatic electrodeposition at -3.40 V and -3.60 V consisted mainly of Nd metal, indicating that this cathodic peak was ascribed to the reduction reaction of $[Nd(TFSA)_5]^{2-}$ in $[P_{2225}][TFSA]$ according to the following reaction:



On the other hand, no anodic peaks corresponding to the oxidation of Nd(0) were apparent in this voltammogram, suggesting that the reduction of $[Nd(TFSA)_5]^{2-}$ is

Fig. 6.13 Cyclic voltammogram of $0.5 \text{ mol dm}^{-3} [Nd(TFSA)_5]^{2-}$ in $[P_{2225}][TFSA]$ at 353 K on a Pt electrode with different scan rates: (a) 5 mV s^{-1} , (b) 10 mV s^{-1} , and (c) 20 mV s^{-1}



an irreversible reaction. A more detailed analysis of this irreversible reaction is presented below.

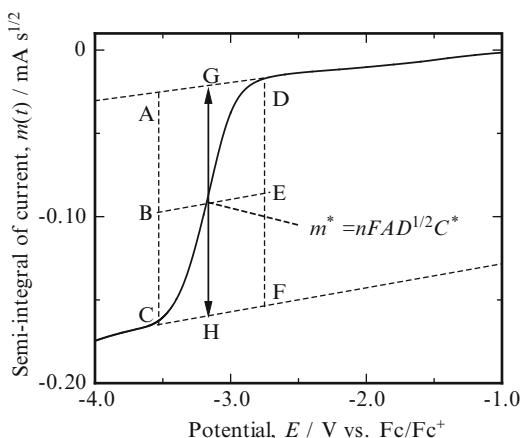
Elucidation of the reduction behavior of $[\text{Nd}(\text{TFSA})_5]^{2-}$ in $[\text{P}_{2225}][\text{TFSA}]$ as well as the diffusion behavior is necessary in order to perform the electrodeposition of Nd metal in $[\text{P}_{2225}][\text{TFSA}]$; thus, we evaluated the diffusion coefficient of $[\text{Nd}(\text{TFSA})_5]^{2-}$ in $[\text{P}_{2225}][\text{TFSA}]$. The diffusion coefficient of $[\text{Nd}(\text{TFSA})_5]^{2-}$ in $[\text{P}_{2225}][\text{TFSA}]$ was calculated from semi-integral (SI) and semi-differential (SD) analyses. Initially, the SI curve was obtained from convolution analysis of the cyclic voltammogram for 0.5 mol dm^{-3} $[\text{Nd}(\text{TFSA})_5]^{2-}$ in $[\text{P}_{2225}][\text{TFSA}]$ using a Pt electrode at 353 K, as shown in Fig. 6.14. An empirical graphical procedure [35] was applied for the determination of the limiting current, m^* , where the vertical lines AC and DF were traced and the mid-points B and E were located. The value of m^* is represented by GH at the potential $E_{1/2}$, which corresponds to the point where the dashed line BE intersects the SI curve. The diffusion coefficient of $[\text{Nd}(\text{TFSA})_5]^{2-}$ was calculated from the value of the limiting current m^* according to the following equation [36]:

$$m^* = nFAD_O^{1/2}C_O^* \quad (6.7)$$

where n is the number of electrons involved in the charge transfer reaction, F is the Faraday constant, A is the electrode surface area, and C^* is the bulk concentration of the electroactive species. The diffusion coefficient of $[\text{Nd}(\text{TFSA})_5]^{2-}$ in $[\text{P}_{2225}][\text{TFSA}]$ at 353 K was evaluated as $1.32 \times 10^{-13} \text{ m}^2 \text{ s}^{-1}$ from SI analysis. Furthermore, the standard rate constant, k_s , can be obtained by using the following equation [36]:

$$E = E_s + \frac{RT}{anF} \ln\left(\frac{k_s}{D_O^{1/2}}\right) + \frac{RT}{anF} \ln\left(\frac{m^* - m(t)}{i(t)}\right) \quad (6.8)$$

Fig. 6.14 Semi-integral curve obtained from the voltammogram of 0.5 mol dm^{-3} $[\text{Nd}(\text{TFSA})_5]^{2-}$ in $[\text{P}_{2225}][\text{TFSA}]$ at 353 K on a Pt electrode with scan rate: 10 mV s^{-1}



where E is the electrode potential, E_s is the standard reversible potential of the reaction, R is the gas constant, T is the thermodynamic temperature, α is the transfer coefficient, m is the current semi-integral, and i is the faradaic current.

The value of αn was calculated from the slope of the E vs. $\log[m^*-m(t)]/i(t)$ plots, and that of k_s can be found from the intercept of the plots. Matsuda and Ayabe reported that in the case of the irreversible reaction, the following equation was satisfied [37]:

$$k_s/(D\nu nF/RT)^{1/2} < 10^{-2(1+\alpha)} \quad (6.9)$$

where ν is the potential scan rate. Therefore, the following relation was obtained by deformation with substitution of the above equation:

$$k_s < 6.85 \times 10^{-6} \text{ cm s}^{-1} \quad (6.10)$$

The k_s value calculated from the intercept of the E vs. $\log[m^*-m(t)]/i(t)$ plots was $1.77 \times 10^{-8} \text{ cm s}^{-1}$. Accordingly, the reduction reaction of $[\text{Nd}(\text{TFSA})_5]^{2-}$ in $[\text{P}_{2225}][\text{TFSA}]$ on the Pt electrode at 353 K was deduced to be an irreversible process.

SD analysis was applied to the cyclic voltammogram of $0.5 \text{ mol dm}^{-3} [\text{Nd}(\text{TFSA})_5]^{2-}$ in $[\text{P}_{2225}][\text{TFSA}]$; the SD curve is shown in Fig. 6.15. The value of W_p , the width of a derivative neopolarographic peak at half its height, and e_p , the current semi-derivative at the peak of the derivative neopolarogram, were determined by SD analysis of the cyclic voltammogram. The diffusion coefficient of $[\text{Nd}(\text{TFSA})_5]^{2-}$ was calculated using the following equations [38] that were established in the case of the irreversible reaction:

Fig. 6.15 Semi-differential curve obtained from the voltammogram of $0.5 \text{ mol dm}^{-3} [\text{Nd}(\text{TFSA})_5]^{2-}$ in $[\text{P}_{2225}][\text{TFSA}]$ at 353 K on a Pt electrode with scan rate: 10 mV s^{-1}

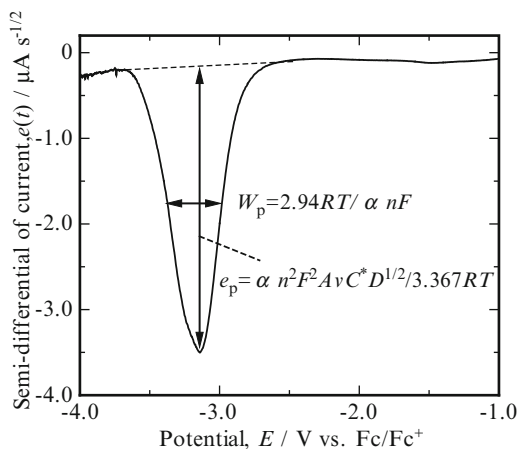


Fig. 6.16 Arrhenius plot of the diffusion coefficients for (a) $[\text{Nd}(\text{TFSA})_5]^{2-}$, (b) $[\text{Dy}(\text{TFSA})_5]^{2-}$, (c) $[\text{Ni}(\text{TFSA})_3]^-$, and (d) $[\text{Fe}(\text{TFSA})_3]^-$ in $[\text{P}_{2225}][\text{TFSA}]$

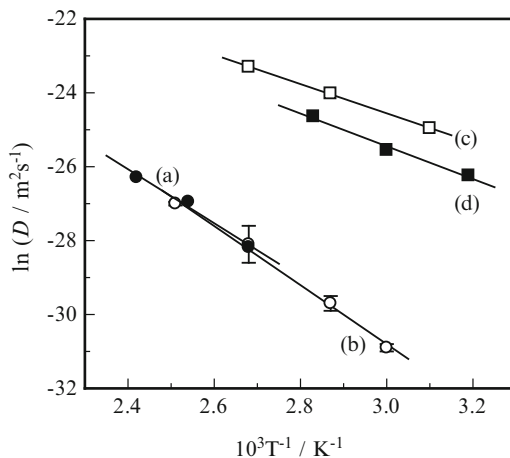


Table 6.2 The activation energy of diffusion coefficient and the solvation number

| | $E_{A,D}/\text{kJ mol}^{-1}$ | Solvation number at 298 K | Solvation number at 423 K |
|-----------------------------------|------------------------------|---------------------------|---------------------------|
| $[\text{Nd}(\text{TFSA})_5]^{2-}$ | 52.8 | 5.1 | 5.0 |
| $[\text{Dy}(\text{TFSA})_5]^{2-}$ | 53.4 | 5.0 | 5.1 |
| $[\text{Fe}(\text{TFSA})_3]^{2-}$ | 26.3 | 3.1 | 3.1 |
| $[\text{Ni}(\text{TFSA})_3]^{2-}$ | 26.0 | 2.6 | 3.3 |

For each metallic complex in $[\text{P}_{2225}][\text{TFSA}]$

$$W_p = 2.94RT/anF \quad (6.11)$$

$$e_p = an^2F^2AvC_O^*D_O^{1/2}/3.367RT \quad (6.12)$$

The diffusion coefficient of $[\text{Nd}(\text{TFSA})_5]^{2-}$ in $[\text{P}_{2225}][\text{TFSA}]$ at 353 K was evaluated as $1.46 \times 10^{-13} \text{ m}^2 \text{ s}^{-1}$ based on SD analysis, which is close to the value derived from SI analysis. This congruence suggests high reliability of the calculated diffusion coefficients of $[\text{Nd}(\text{TFSA})_5]^{2-}$ in $[\text{P}_{2225}][\text{TFSA}]$ at 353 K derived from SI and SD analyses. The Arrhenius plot of the diffusion behavior for $[\text{Nd}(\text{TFSA})_5]^{2-}$ in $[\text{P}_{2225}][\text{TFSA}]$ is presented in Fig. 6.16. The D values of $[\text{Nd}(\text{TFSA})_5]^{2-}$ [16], $[\text{Dy}(\text{TFSA})_5]^{2-}$ [20], $[\text{Fe}(\text{TFSA})_3]^{2-}$, and $[\text{Ni}(\text{TFSA})_3]^{2-}$ in $[\text{P}_{2225}][\text{TFSA}]$ from our previous investigations are also displayed in Fig. 6.16 for comparative purposes. The activation energy of the diffusion process was tabulated in Table 6.2 with the solvation number of each metallic complex. The activation energy of $[\text{Nd}(\text{TFSA})_5]^{2-}$ or $[\text{Dy}(\text{TFSA})_5]^{2-}$ was found to be larger than that of $[\text{Fe}(\text{TFSA})_3]^{2-}$ or $[\text{Ni}(\text{TFSA})_3]^{2-}$. The difference of $E_{A,D}$ value between the RE complex and iron group metallic complex is explained from the complexation between each centered metallic cation and the surrounding $[\text{TFSA}]^-$ anion ligand.

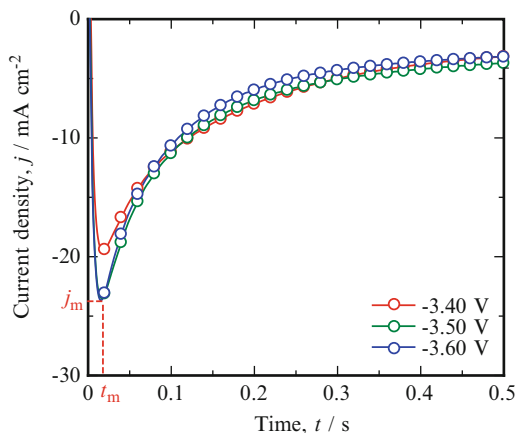


Fig. 6.17 Chronoamperogram on a Pt electrode for $0.5 \text{ mol dm}^{-3} [\text{Nd}(\text{TFSA})_5]^{2-}$ in $[\text{P}_{2225}][\text{TFSA}]$ at 353 K

6.5.2 Nucleation Behavior of Nd Nuclei

The initial nucleation and the growth behavior of Nd nuclei in $[\text{P}_{2225}][\text{TFSA}]$ were investigated by means of chronoamperometry. A characteristic peak of the nucleation process was observed just after the initial current decay corresponding to the charging of the electric double layer. This peak is indicative of the three-dimensional (3D) growth of the Nd nuclei; there was an initial increase in the faradaic current due to nucleation and the growth of the Nd nuclei that involves an increase of the electroactive area; eventually a current maximum, j_m , was achieved at time t_m ; finally, this current quickly decayed to a diffusion limited current. Chronoamperograms were recorded at the Pt electrode as shown in Fig. 6.17.

For these chronoamperograms, the charging current of neat $[\text{P}_{2225}][\text{TFSA}]$ was deduced from the data for $[\text{P}_{2225}][\text{TFSA}]$ containing $0.5 \text{ mol dm}^{-3} [\text{Nd}(\text{TFSA})_5]^{2-}$ in order to analyze the faradaic current only in the reduction reaction of $[\text{Nd}(\text{TFSA})_5]^{2-}$. Several models have been developed to describe the $j-t$ curves for metal deposition. It has been previously reported that the theoretical methodology developed by Scharifker and Hills [39] is applicable to the deposition of several metals from TFSA-based ILs [40–44]. Therefore, the initial stage of the nucleation and the crystal growth of Nd were analyzed by using the Hills–Scharifker method in this study. The previously mentioned study reported that 3D nucleation on an electrode surface can be classified into instantaneous and progressive nucleation. In the case of the instantaneous nucleation, the nuclei are deposited on the electrode surface and grow at a constant rate that is dependent on the applied potential. The resultant $j-t$ curves are mathematically described by the following equation:

$$\left(\frac{j}{j_m}\right)^2 = \frac{1.2254}{t/t_m} \left\{ 1 - \exp \left[-2.3367 \left(\frac{t}{t_m}\right)^2 \right] \right\}^2 \quad (6.13)$$

where j is the current density at time t and j_m is the maximum current density at time t_m . In the case of the progressive nucleation, the initially deposited nuclei grow at varying rates dependent on the time of deposition. The j - t curves can be mathematically described by the following equation:

$$\left(\frac{j}{j_m}\right)^2 = \frac{1.9542}{t/t_m} \left\{ 1 - \exp \left[-1.2564 \left(\frac{t}{t_m}\right) \right] \right\}^2 \quad (6.14)$$

The relationship between the squared dimensionless current density and the dimensionless time of $[\text{Nd}(\text{TFSA})_5]^{2-}$ in $[\text{P}_{2225}][\text{TFSA}]$ is shown in Fig. 6.18, along with the theoretical curves derived from Eqs. (6.13) and (6.14). When the overpotential at -3.40 V was applied, the experimental data were consistent with the instantaneous nucleation model. On the other hand, when the applied potentials were -3.50 V and -3.60 V, the experimental data shifted from that of the instantaneous nucleation model to the progressive nucleation model. These results indicated that the nucleation mechanism changed depending on the applied potential. These nucleation behaviors would be related to the number density of active sites and the nucleation rates per site from the current transients [45] as will be discussed later. This alternation from instantaneous to progressive nucleation was consistent with the nucleation mechanism for Dy in $0.1 \text{ mol dm}^{-3} [\text{Dy}(\text{TFSA})_5]^{2-}$ in $[\text{P}_{2225}][\text{TFSA}]$ [20]. The initial nucleation and the crystal growth processes would influence the formation of the electrodeposits in the initial stage of the electrodeposition. Accordingly, consideration of the applied potential is important for achieving electrodeposits with the desired morphology and quality from the electrodeposition process.

Fig. 6.18 $(j/j_m)^2$ - t/t_m plots for 0.5 mol dm^{-3} $[\text{Nd}(\text{TFSA})_5]^{2-}$ in $[\text{P}_{2225}][\text{TFSA}]$ evaluated from CA

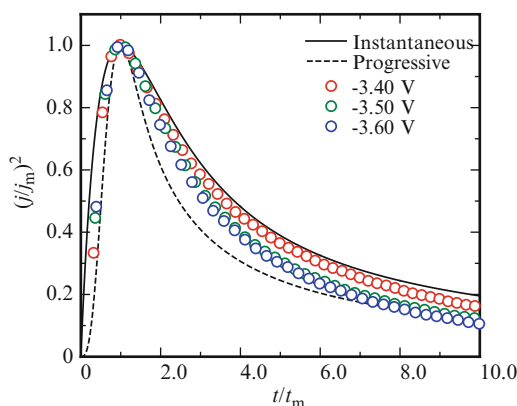


Table 6.3 The nucleation number density of Nd nuclei from j - t curves at each applied potential in [P₂₂₂₅][TFSA] including 0.5 mol dm⁻³ [Nd(TFSA)₅]²⁻

| Applied potential (E)/V | -3.40 | -3.50 | -3.60 |
|-------------------------------------------------------------|-------|-------|-------|
| Nucleation number density ($10^{11}N_0$)/cm ⁻² | 2.0 | 1.7 | 1.7 |

The number density of nuclei was also investigated as follows: the nucleation number density, N_0 , can be calculated from the maximum current, j_{\max} , and time, t_{\max} , of the j - t curve based on the following equation [45]:

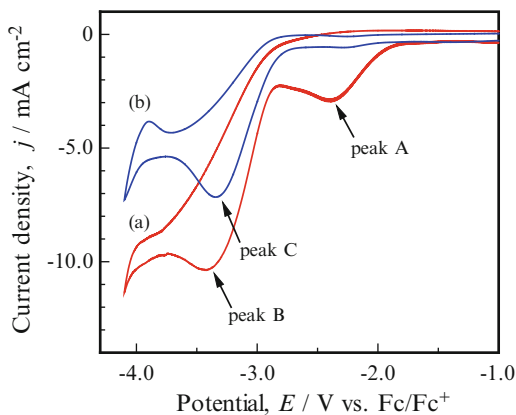
$$N_0 = 0.065(8\pi C_O^* M/\rho)^{-1/2} (nFC_O^*/j_{\max} t_{\max})^2 \quad (6.15)$$

where M and ρ are the atomic mass and the density of the deposited metal, respectively. During the initial stages of deposition, well before the maxima in the j - t curves, the initial nucleation can be considered to be effectively instantaneous, i.e., all nuclei may be considered to have been formed at the same time [46]. Thus, in the analysis of the data from the very early portion of the current transient, Eq. (6.15) can be used to evaluate the value of N_0 for all systems studied. The number of Nd nuclei formed during the very early stages of nucleation was estimated using this methodology; the data are presented in Table 6.3. In general, the nucleation number density would increase with increasing overpotential on stable progressive nucleation, e.g., the nucleation of Sn nuclei in 1-ethyl-3-methylimidazolium chloride-tetrafluoroborate, [C₂C₁Im][Cl, BF₄] [47]. However, contrary to our expectations, the number density of Nd nuclei at the initial stage of the nucleation decreased as the overpotential increased from -3.40 V to -3.50 V or -3.60 V in this study. These tendencies would be related with the alternation from instantaneous to progressive nucleation. It was reported that the rate of nucleation was changed by the overpotential for instantaneous or progressive nucleation [48]. Thus, the different nucleation rates on instantaneous or progressive nucleation would be affected for the nucleation number density. The nucleation mechanism of Nd and Dy [20] revealed that the number density of nuclei is dependent on the overpotential, suggesting that the applied potential for electrodeposition becomes an important factor from the perspective of the nucleation mechanism as well as the number of nuclei.

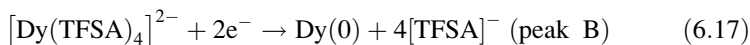
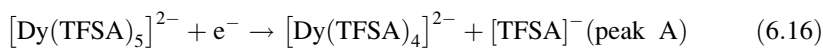
6.5.3 Electrochemical Behavior of Dy(II) and Dy(III)

The voltammetric analysis of 0.1 mol dm⁻³ [Dy(TFSA)₅]²⁻ in [P₂₂₂₅][TFSA] was performed with various scan rates at different fractions of water content. The cyclic voltammogram of 0.1 mol dm⁻³ [Dy(TFSA)₅]²⁻ in [P₂₂₂₅][TFSA] with 0.1 V s⁻¹ at 363 K is shown in Fig. 6.19. The voltammograms shown in Fig. 6.19a, b contained 98 and 203 ppm water in the IL, respectively. No anodic peaks corresponding to the oxidation of Dy(0) were observed in any voltammogram. This result suggests that

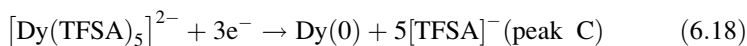
Fig. 6.19 The cyclic voltammogram of $0.1 \text{ mol dm}^{-3} [\text{Dy}(\text{TFSA})_5]^{2-}$ in $[\text{P}_{2225}][\text{TFSA}]$ at 363 K with different water contents, (a) 98 ppm and (b) 203 ppm (Reprinted with permission from Ref. [21] Copyright 2013, Elsevier Science)



the reduction of $[\text{Dy}(\text{TFSA})_5]^{2-}$ is an irreversible process. There was no oxidation peak of $\text{Dy}(0)$ in DMF and DMPT bath, and this reduction process of Dy complex was an irreversible reaction [14]. Regarding the cathodic peaks, a remarkable difference in the reduction process appeared between two samples with different water contents, as shown in Fig. 6.19. In the case of a small amount of water (98 ppm) in IL (Fig. 6.19a), there were two reduction peaks around -2.4 and -3.5 V in the voltammogram. In contrast, there was only one reduction peak around -3.6 V for the sample with a relatively large amount of water content (203 ppm; Fig. 6.19b). This result suggests that water molecules in the electrolyte remarkably influenced the reduction process of $[\text{Dy}(\text{TFSA})_5]^{2-}$ in $[\text{P}_{2225}][\text{TFSA}]$. For a small amount of water in the IL, the reduction peak A at approximately -2.4 V and the reduction peak B at approximately -3.5 V are expressed for the following two-step reactions:



On the other hand, for an increased amount of water in IL, the reduction reaction of $[\text{Dy}(\text{TFSA})_5]^{2-}$ proceeds in one step by the following reaction:



The latter one-step reduction reaction is consistent with our recent electrochemical investigation into $[\text{Dy}(\text{TFSA})_5]^{2-}$ [20]. This result indicated that the presence of the water molecule and the solvation structure of ILs is related to the reduction behavior of $[\text{Dy}(\text{TFSA})_4]^{2-}$ and $[\text{Dy}(\text{TFSA})_5]^{2-}$. According to Raman spectroscopy [18], the solvation number of $[\text{Nd}(\text{TFSA})_5]^{2-}$ in $[\text{P}_{2225}][\text{TFSA}]$ is 5.1. Raman spectroscopy has also revealed that five $[\text{TFSA}]^-$ anions act as a bidentate ligand as its two O atoms are centered around the $[\text{Nd}^{3+}]$ ion in the TFSA-based ILs. Similar

coordination structures with a multianion $[\text{TFSA}]^-$ bidentate ligand have already been demonstrated from DFT calculations in our recent study [49]. The coordination structure for $[\text{Dy}(\text{TFSA})_5]^{2-}$ in $[\text{P}_{2225}][\text{TFSA}]$ was confirmed to have similar tendencies. However, if there were a relatively large amount of H_2O molecules in the TFSA-based ILs, the O atoms of H_2O molecules would preferentially coordinate with the centered $[\text{Dy}^{3+}]$ ion because, as per the spectrochemical series, the strength of O atoms in H_2O is greater than those of $[\text{TFSA}]^-$ anions. Thus, when an aqua complex such as $[\text{Dy}(\text{H}_2\text{O})_9]^{3+}$ forms in ILs with a relatively large number of H_2O molecules, a larger overpotential is necessary for the reduction of the Dy–aqua complex when compared to the Dy–TFSA complex. Therefore, no intermediate reduction reaction from $[\text{Dy}(\text{TFSA})_5]^{2-}$ to $[\text{Dy}(\text{TFSA})_4]^{2-}$ occurs in ILs with 203 ppm water. In addition, a remarkable difference in the peak current density (j_p^{red}) at the electrodeposition potential of Dy(0) was observed in the voltammograms shown in Fig. 6.19. The values of j_p^{red} for samples containing 98 and 203 ppm water were -10.4 and -7.2 mA cm^{-2} , respectively. This increase in the current density contributes to the increase in the current efficiency of Dy electrodeposition. In conclusion, we revealed that $[\text{Dy}(\text{TFSA})_5]^{2-}$ dissolved in $[\text{P}_{2225}][\text{TFSA}]$ was electrodeposited in a two-step reduction process by way of $[\text{Dy}(\text{TFSA})_4]^{2-}$ in an IL system containing less than 100 ppm water.

Assuming each peak on CV is based on the cathodic reactions (6.16) and (6.17), we confirmed that the cathodic peak plot of the current density (j_p) vs. the square root of the potential scan rate ($v^{1/2}$) demonstrated a strong linear relationship. This result indicates that both the reduction reactions, (6.16) and (6.17), using a Pt electrode, were controlled by diffusion, i.e., mass transport under semi-infinite linear diffusion conditions. In addition, the slope of the j_p vs. $v^{1/2}$ plot is different between the two reactions, which suggests that there is a difference in the diffusion coefficient of each electrochemical species, $[\text{Dy}(\text{TFSA})_4]^{2-}$ and $[\text{Dy}(\text{TFSA})_5]^{2-}$. Therefore, the diffusion coefficients of $[\text{Dy}(\text{TFSA})_4]^{2-}$ and $[\text{Dy}(\text{TFSA})_5]^{2-}$ in $[\text{P}_{2225}][\text{TFSA}]$ were estimated from the SI analysis of the voltammogram. When discussing the rate of the electrode reaction, both mass transfer and charge transfer processes are very important. In particular, mass transfer by diffusion is a principal factor in deciding the aspects of the electrode reaction, particularly in IL solvents. Therefore, it is necessary to evaluate the diffusion coefficients of $[\text{Dy}(\text{TFSA})_4]^{2-}$ and $[\text{Dy}(\text{TFSA})_5]^{2-}$ in $[\text{P}_{2225}][\text{TFSA}]$ when considering the electrodeposition of the Dy metal. Analyzing the SI limiting current enabled us to more accurately evaluate the diffusion coefficients of $[\text{Dy}(\text{TFSA})_4]^{2-}$ and $[\text{Dy}(\text{TFSA})_5]^{2-}$ in an irreversible process. The SI curves obtained from the voltammogram of 0.1 mol dm^{-3} (water content: 98 ppm) $[\text{Dy}(\text{TFSA})_5]^{2-}$ in $[\text{P}_{2225}][\text{TFSA}]$ at 363 K are shown in Fig. 6.20. The values of m_1^* and m_2^* were conventionally determined by subtracting the background current. The diffusion coefficients of $[\text{Dy}(\text{TFSA})_4]^{2-}$ and $[\text{Dy}(\text{TFSA})_5]^{2-}$ were, respectively, calculated from the values of m_1^* and m_2^* based on Eq. (6.7) [31]. The diffusion coefficients of $[\text{Dy}(\text{TFSA})_5]^{2-}$ obtained for a 0.1 M in $[\text{P}_{2225}][\text{TFSA}]$ solution were in the same order as those of 7.5×10^{-2} and 0.5 mol dm^{-3} $[\text{Dy}(\text{TFSA})_5]^{2-}$, as described in our recent electrochemical analyses [12]. In addition, we revealed that the diffusion coefficients of $[\text{Dy}(\text{TFSA})_4]^{2-}$ were larger

Fig. 6.20 The semi-integrated curves obtained from the voltammogram of 0.1 mol dm^{-3} $[\text{Dy}(\text{TFSA})_5]^{2-}$ in $[\text{P}_{2225}][\text{TFSA}]$ (water content: 98 ppm) at 363 K (Reprinted with permission from Ref. [21] Copyright 2013, Elsevier Science)

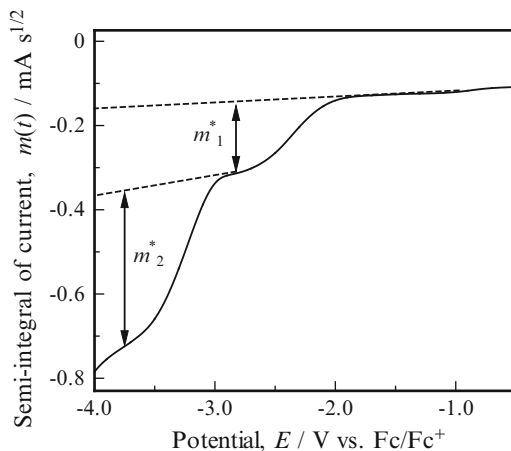
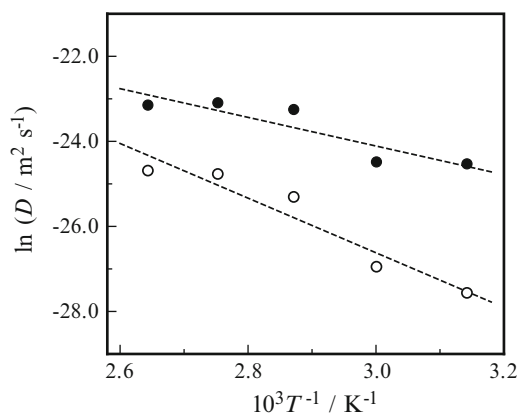


Fig. 6.21 Arrhenius plots for the diffusion coefficients of $[\text{Dy}(\text{TFSA})_4]^{2-}$ and $[\text{Dy}(\text{TFSA})_5]^{2-}$ in $[\text{P}_{2225}][\text{TFSA}]$, \bullet : $[\text{Dy}(\text{TFSA})_4]^{2-}$ and \circ : $[\text{Dy}(\text{TFSA})_5]^{2-}$ (Reprinted with permission from Ref. [21] Copyright 2013, Elsevier Science)



than those of $[\text{Dy}(\text{TFSA})_5]^{2-}$ in the entire range of temperatures measured, which indicates that the coordination number of TFSA anions around the centered Dy^{3+} ion for $[\text{Dy}(\text{TFSA})_4]^{2-}$ is smaller than that of $[\text{Dy}(\text{TFSA})_5]^{2-}$ because of the electrostatic interaction between the cation and the anion.

We then evaluated the activation energy for diffusion ($E_{A,D}$) using diffusion coefficient values with temperature dependence. The transfer of metallic cations in the electrolytic solution is generally affected by their electrostatic interaction with the ions constituting the metal complexes. Therefore, the diffusion of metallic cations in ILs needs more activation energy than the dissociation energy associated with the anions surrounding the metal complexes. The $E_{A,D}$ value is given by the Arrhenius rule:

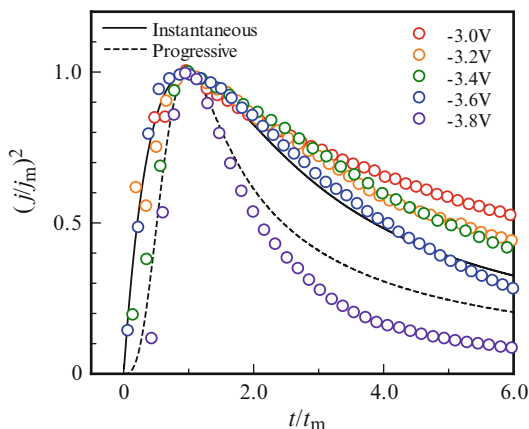
$$D_0 = A^* \exp(-E_{A,D}/RT) \quad (6.19)$$

where A^* is the frequency factor. The Arrhenius plot, a logarithmic plot of the diffusion coefficient for $[\text{Dy}(\text{TFSA})_4]^{2-}$ and $[\text{Dy}(\text{TFSA})_5]^{2-}$ against the inverse of the temperature, is shown in Fig. 6.21. The $E_{A,D}$ values determined from Eq.(6.19) for $[\text{Dy}(\text{TFSA})_4]^{2-}$ and $[\text{Dy}(\text{TFSA})_5]^{2-}$ in $[\text{P}_{2225}][\text{TFSA}]$ were 28.0 and 53.4 kJ mol⁻¹, respectively. The observation that the $E_{A,D}$ value of $[\text{Dy}(\text{TFSA})_4]^{2-}$ is smaller than that of $[\text{Dy}(\text{TFSA})_5]^{2-}$ is consistent with the tendency of the diffusion coefficient estimated from the slope of the j_p vs. $v^{1/2}$ plot. This result indicates that the electrostatic interaction of $[\text{Dy}(\text{TFSA})_4]^{2-}$ with $[\text{TFSA}]^-$ anions is weaker than that of $[\text{Dy}(\text{TFSA})_5]^{2-}$ because of smaller coulombic interactions and also that the total electrodeposition energy of the Dy metal would lead to smaller energy consumption.

6.5.4 Nucleation Behavior of Dy Nuclei

The CA responses at different overpotentials were measured to analyze the nucleation and nuclear growth mechanism. For these chronoamperograms, the charging current of neat $[\text{P}_{2225}][\text{TFSA}]$ was deducted from the data of $[\text{P}_{2225}][\text{TFSA}]$, along with that of $[\text{Dy}(\text{TFSA})_5]^{2-}$, in order to analyze only the faradaic current in the reduction reaction of $[\text{Dy}(\text{TFSA})_5]^{2-}$. The CA curves for the potential values close to E_p^{red} indicated that the faradaic current increased because of the nucleation and growth of the Dy nuclei; eventually, this increasing current reached a maximum, j_m , at time t_m , which was attributed to the 3D growth of the Dy metal over the nuclei, resulting in an increase in the surface area. Finally, this current decayed because of the increase in the thickness of the diffusion layer after reaching the maximum. Several models to describe the $j-t$ curves for metal electrodeposition have also been developed. It has been previously reported that the theoretical methodology developed by Scharifker and Hills [39] is applicable to several metals dissolved in TFSA-based ILs [40–44]. Therefore, we analyzed the nucleation and crystal growth of Dy electrodeposition in $[\text{P}_{2225}][\text{TFSA}]$ by the Hills–Scharifker method. According to this report, the nucleation process is described by two limiting cases, instantaneous and progressive nucleation mechanisms. In the case of instantaneous nucleation, the nucleation particles are electrodeposited on the electrode surface and grown at a constant rate, which is dependent on the applied overpotential. In this nucleation process, the $j-t$ curves can be mathematically described by Eqs. (6.13) and (6.14). In the case of the progressive nucleation, the electrodeposited nuclei proceed at various rates depending on the electrodeposition time. The resultant $j-t$ curves are described by Eq.(6.13). The relationship between the squared dimensionless current density $(j/j_m)^2$ and the dimensionless time (t/t_m) for Dy nuclei in $[\text{P}_{2225}][\text{TFSA}]$ is shown in Fig. 6.22, with theoretical curves. When the overpotential of -3.6 V is applied, the nucleation behavior obeyed the instantaneous nucleation model. On the other hand, the nucleation curve at -3.8 V is followed by the progressive nucleation model. This result indicates that the nucleation mechanism of Dy changed, depending on the applied overpotential. At overpotential values close to the onset potential for Dy electrodeposition, instantaneous nucleation and growth occurs; however, as the overpotential becomes more negative than E_p^{red} on the

Fig. 6.22 $(j/j_m)^2-t/t_m$ plots for 0.1 mol dm^{-3} [Dy(TFSA) $_5$] $^{2-}$ in [P $_{2225}$] [TFSA] with different overpotentials evaluated from CA (Reprinted with permission from Ref. [21] Copyright 2013, Elsevier Science)



voltammogram, the process changes to progressive nucleation and growth. This alteration of nucleation behavior under different applied overpotential values was also reported for Ag electrodeposition in *N*-butyl-*N*-methyl-pyrrolidinium bis(trifluoromethyl-sulfonyl)amide, [C $_4$ C $_1$ Py][TFSA] [43]. Moreover, it has been reported that progressive nucleation occurred for both Pd [40] and Sn [41] in 1-*n*-butyl-1-methylpyrrolidinium bis(trifluoromethyl-sulfonyl)amide, [BMP][TFSA], when the induced overpotential values were more negative than the reduction peak potential (E_p^{red}) on the voltammogram, and that instantaneous nucleation proceeded for Ni [42] in [BMP][TFSA] when an overpotential more positive than E_p^{red} was applied. After all, the nucleation behavior in TFSA-based ILs is controlled by the applied overpotentials and is independent of the specific metallic species. This difference in the nucleation mechanism would also be greatly influenced by the formation of the electrodeposit in the initial stages of electrodeposition. Therefore, by applying an overpotential based on the desired nucleation mechanism, the morphology and quality of electrodeposits could be improved by the electrodeposition process. In the following section, we discuss the actual Dy electrodeposition under potentiostatic conditions at -3.8 V , which led to preferentially progressive nucleation.

6.6 Electrodeposition of Nd and Dy Metals

6.6.1 Electrodeposition of Nd Metal

Electrodeposition at -3.40 V produced blackish electrodeposits on the Cu substrate. The total transported charge was 178.4 C . The SEM image of the electrodeposits obtained by electrodeposition at -3.40 V was shown in Fig. 6.23. The morphology of both electrodeposits was granular with a nonuniform size

Fig. 6.23 The SEM images of deposits obtained by electrodeposition performed at -3.40 V

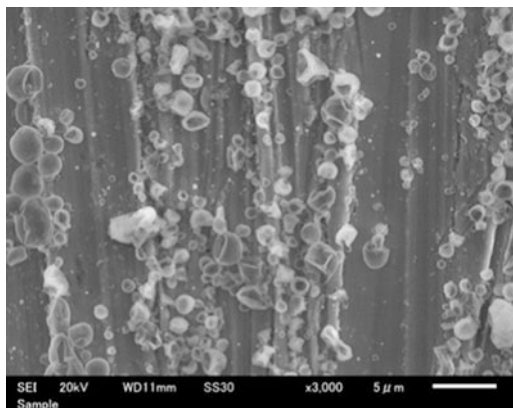
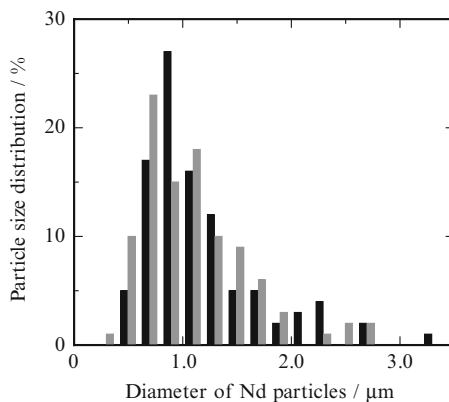


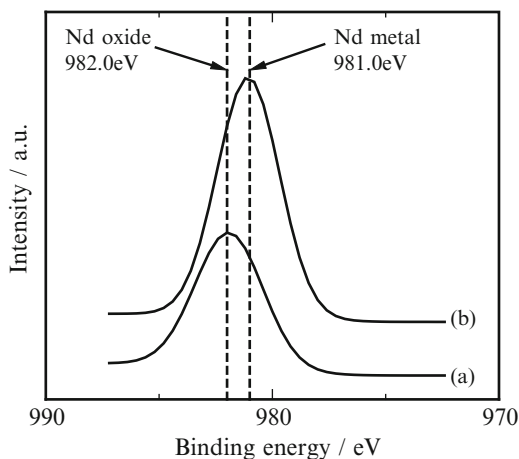
Fig. 6.24 The size distribution of the electrodeposited Nd particles. *Black*: Nd particle size distribution of -3.40 V. *Gray*: Nd particle size distribution of -3.60 V



distribution. This morphology is considered to be generated because the initial stage of nucleation and growth occurred according to the progressive nucleation model in which the nucleation rate was faster than the crystal growth rate. As shown in Fig. 6.22, at -3.40 V, the $j-t$ curve could be fitted to the theoretical curve for instantaneous nucleation at the early stage, but the curve slowly shifted to conform to the progressive nucleation model as time elapsed. Furthermore, the initial nucleation data gradually approached the theoretical curve for the progressive nucleation model with time. Therefore, the results of the electrodeposition experiments are consistent with the data for initial nucleation and growth of Nd in [P₂₂₂₅] [TFSA] by CA discussed above. The particle size distribution of the Nd grains obtained at -3.40 V and -3.60 V is displayed in Fig. 6.24. With the use of applied potentials of -3.40 V and -3.60 V, the average diameters of the Nd particles were 1.17 μm and 1.08 μm , respectively. The particle size of the electrodeposits obtained by electrodeposition at -3.60 V was smaller than that achieved at -3.40 V. The number of particles deposited at -3.60 V was also larger than that at -3.40 V. These results were also consistent with the results obtained by CA, which

Table 6.4 The composition of electrodeposits on Cu substrate obtained by electrodeposition performed at -3.40 V and -3.60 V from 0.5 M $[\text{Nd}(\text{TfSA})_5]^{2-}$ in $[\text{P}_{2225}][\text{TfSA}]$ at 353 K

| Elements | | C | N | O | F | S | Fe | Nd |
|----------|-----------|------|------|-------|------|------|------|-------|
| wt. % | -3.40 V | 1.78 | 1.02 | 18.26 | 4.24 | 2.74 | 0.00 | 71.96 |
| | -3.60 V | 1.92 | 1.47 | 23.34 | 6.72 | 3.92 | 0.00 | 62.63 |

Fig. 6.25 The Nd $3d_{5/2}$ spectra of the electrodeposits by XPS analysis. (a) The surface layer at -0.15 μm of the electrodeposits. (b) The middle layer at -0.75 μm of the electrodeposit

indicated that the number density of Nd nuclei increased with increasing overpotential.

The quantitative analysis data for the electrodeposits obtained by electrodeposition at -3.40 V and -3.60 V using EDX are summarized in Table 6.4. The data demonstrate that the electrodeposits obtained on the Cu substrate at -3.40 V and -3.60 V both comprise mainly Nd. However, a relatively large amount of O was also detected in the electrodeposits, suggesting that Nd would be combined with O. Thus, the chemical bonding state of Nd in the electrodeposits was analyzed by using XPS. Elemental Fe that was dissolved from the anode was hardly detected in the electrodeposits generated at both potentials. Therefore, the separation of the anode from the main electrolyte using the Vycor glass filter was an effective strategy. Decomposition of the main electrolyte was prevented by this electrodeposition cell structure; thus, this cell structure enabled acquisition of Nd in the electrodeposits while preventing bonding with the light elements (C, F, and S) that constitute the ILs.

The Nd $3d_{5/2}$ XPS spectra of the electrodeposits deposited at -3.40 V and -3.60 V were shown in Fig. 6.25(a) and (b), respectively. The surfaces of both electrodeposits were sputtered using an Ar ion beam to facilitate in-depth analysis of the surface and the middle layer, that is, (a) -0.15 μm and (b) -0.75 μm , of the electrodeposits. Theoretically, the binding energy of Nd $3d_{5/2}$ for metallic Nd and oxides should be positioned at 980.5 – 981.0 eV and 981.7 – 982.3 eV, respectively, with the use of the monochromated Al $K\alpha$ line [50]. The peak maxima in the Nd $3d_{5/2}$ spectra acquired for the layers (a) under 150 nm and (b) under 50 nm were

detected at 981.57 eV and 982.25 eV, respectively. Hence, the Nd species obtained by electrodeposition using $[P_{2225}][TFSA]$ were identified as Nd metal and oxide mixtures. It is thought that metallic Nd should initially be electrodeposited on the Cu substrate and subsequently oxidized by the O components in the electrolyte, that is, water or dissolved oxygen. It has been reported that the water content of the electrolyte did not significantly affect the oxidation state of the electrodeposits, but may influence the coordination number of the Nd complex and the diffusion behavior. Therefore, sufficient dehydration and control of the water content of the electrolyte are important points for achieving high-purity metallic Nd.

6.6.2 Electrodeposition of Dy Metal

In the electrodeposition experiments, a Cu substrate and a prismatic Nd–Fe–B rod were used as a cathode and an anode, respectively. A platinum QRE was used for this electrodeposition system because the applied overpotential was precisely induced on both electrodes. The electrodeposition of the Dy metal from $0.1 \text{ mol dm}^{-3} [\text{Dy}(\text{TFSA})_5]^{2-}$ in $[P_{2225}][\text{TFSA}]$ at 393 K was conducted under an Ar atmosphere ($\text{H}_2\text{O} < 1.0 \text{ ppm}$) in a glove box at 393 K. The applied overpotential on the cathode for the potentiostatic electrolysis was set at -3.8 V based on the above nucleation study. The potentiostatic electrolysis was carried out while stirring the electrolyte at 500 rpm in order to increase the current density of electrodeposition by continuously supplying the electroactive species $[\text{Dy}(\text{TFSA})_5]^{2-}$ to the electrode surface.

The average current density and the total transported charge under these electrodeposition conditions were -32.9 mA cm^{-2} and 300 C for 43.6 h, respectively. We confirmed that the decomposition of IL did not occur under these electrodeposition conditions because there was little change in the color of the light-yellow electrolyte before and after electrodeposition. As for the cathode, we confirmed that the blackish-brown electrodeposits had a strong adhesion on the Cu substrate. The microscopic morphology and elemental analysis of the electrodeposited samples of Dy recovered at -3.8 V were examined by SEM/EDX. The SEM image and EDX mapping of the electrodeposits are represented in Fig. 6.26a, b, respectively. The round particles on the Cu substrate were confirmed to be Dy metals and other related compounds.

A quantitative analysis of the electrodeposits is listed in Table 6.5. We confirmed that the greater part of the electrodeposited Dy was composed of the metallic state, because very little oxygen was detected on the surface of the electrodeposited Dy metal using EDX mapping. The amounts of carbon and oxygen detected in EDX came from the Cu substrate. The particle size distribution indicated that metallic Dy particles with ca. $0.8\text{--}0.9 \text{ }\mu\text{m}$ diameter showed a high distribution ratio. In summary, this electrodeposition experiment allowed us to demonstrate that electrodeposited Dy contains a large amount of the metallic state and a smaller amount of the oxide state on the top surface. An in-depth analysis of the

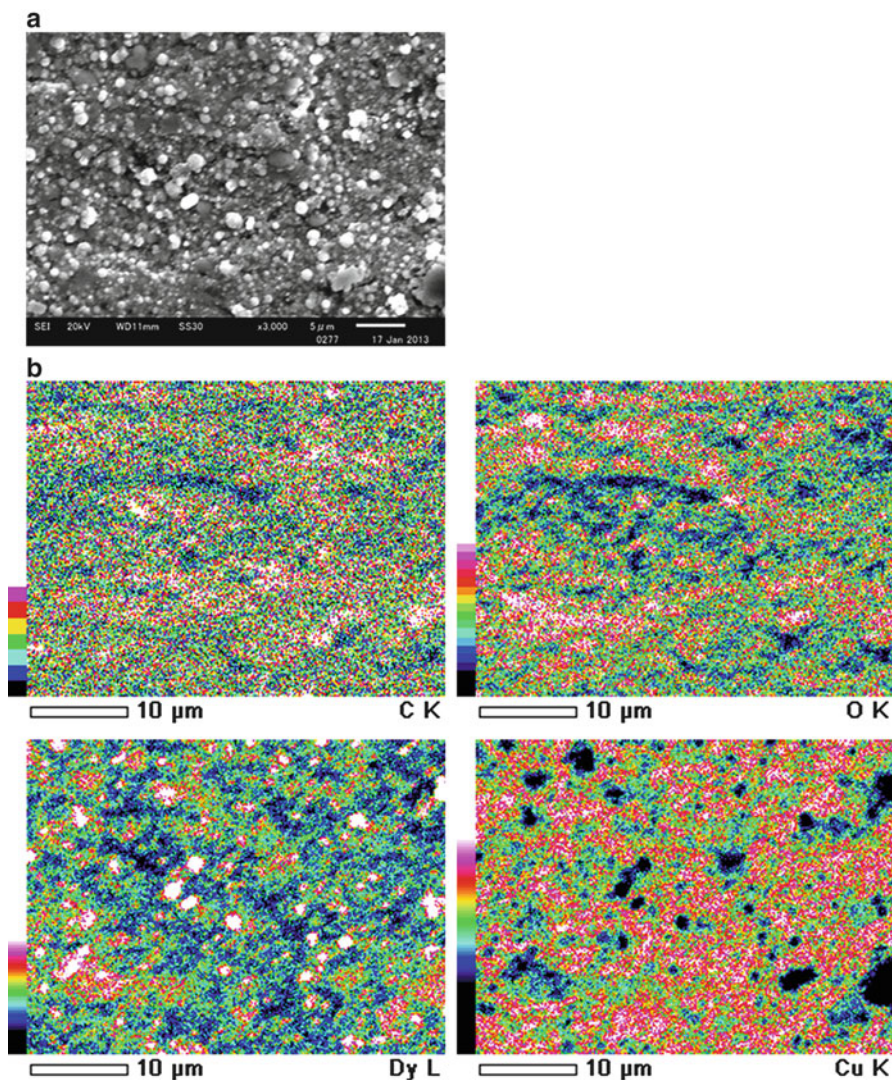
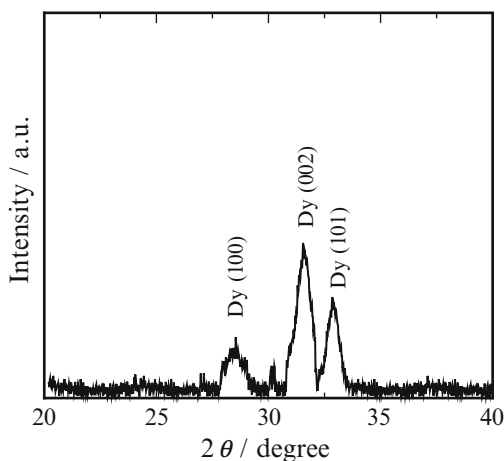


Fig. 6.26 (a) The SEM image and (b) the EDX mapping of the electrodeposited Dy sample on a Cu substrate at -3.8 V from 0.1 mol dm^{-3} $[\text{Dy}(\text{TFSA})_5]^{2-}$ in $[\text{P}_{2225}][\text{TFSA}]$ at 393 K (Reprinted with permission from Ref. [21] Copyright 2013, Elsevier Science)

electrodeposited Dy was conducted with the $\text{Al-K}\alpha$ radiation by XPS. The $\text{Dy}3d_{5/2}$ spectrum for the top surface and the middle layer (under $0.5 \mu\text{m}$) of the electrodeposits is investigated, and the XPS analysis of the inner part of the electrodeposits was performed by Ar sputtering. The sputtering rate was 27.2 nm min^{-1} estimated from the sputtering rate of the Si standard. Theoretically, the $\text{Dy}3d_{5/2}$ peaks for the Dy metal and oxides should be positioned at 1295.8 and 1289.0 eV, respectively

Table 6.5 The quantitative analysis of the electrodeposits under the potentiostatic condition at -3.8 V by EDX

| Elements | C | N | O | F | P | S | Dy | Cu |
|----------|-------|------|-------|------|------|------|------|-------|
| wt. % | 10.83 | 1.15 | 11.82 | 3.87 | 0.86 | 1.87 | 9.27 | 60.33 |

Fig. 6.27 XRD profile of the electrodeposits under potentiostatic electrodeposition at -3.8 V (Reprinted with permission from Ref. [21] Copyright 2013, Elsevier Science)

[50]. The $Dy3d_{5/2}$ peaks of the electrodeposits have a binding energy of 1297.2 eV, which hardly shifted before and after the Ar etching. The $Dy3d_{5/2}$ spectra of the top surface and the middle layer showed a relatively good agreement with the theory. The XRD pattern of the electrodeposits at a low angle is displayed in Fig. 6.27. As shown in this figure, the crystal plane indices of the Dy metallic phase are in good accordance with the JCPDS data. In this study, a series of analyses of Dy electrodeposits enabled us to conclude that most of the metallic state of Dy can be recovered from a phosphonium-based IL by electrodeposition.

6.7 Recovery Process of Nd Metal from Spent Nd–Fe–B Magnets

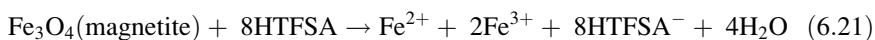
6.7.1 Pretreatment Process

The spent Nd–Fe–B magnet in voice coil motor (VCM) was applied as a starting material for the recovery process. The VCM in a 3.5 inch HDD was dismantled and separated from Al metals. The pretreatment process was constituted of the demagnetization, chemical etching, and roasting treatment. For the demagnetization process, Nd–Fe–B magnet was heated in an electric muffle furnace (FUW220PA, Advantec, Inc.,) at 90 K/h up to Curie temperature: 583 K. The iron yoke in contact with the VCM was dislocated from the RE-containing magnet. The magnetic flux

density of the Nd–Fe–B magnet was measured using a digital TESLA meter (TM-701, Kanetec Co. Ltd.) before and after the demagnetizing treatment. The magnetic flux density before and after this treatment was 440 mT and less than 0.1 mT, respectively. Thus, the demagnetization ratio was performed at 99.9 %. After the demagnetization process, a base solution was prepared to exfoliate Ni layers by mixing ENSTRIP EN-79A, EN-79B (Meltex Inc.), and the NaOH (Wako Pure Chemical Industries, Ltd., >97.0 %) with the distilled water. The demagnetized Nd–Fe–B magnet components in VCM were immersed in the exfoliation solution at 363 K. In the case of Ni–Cu–Ni triple layers on the VCM coating, Cu layers were mechanically polished as necessary. Therefore, Ni–Cu–Ni layers were perfectly removed from the Nd–Fe–B magnet on this chemical etching process. Then, some pieces of Nd–Fe–B magnets were milled by using a grinder (IKA[®]-GMBH & Co. KG, A11) with a cutting tooth (IKA[®]-GMBH & Co. KG, A11.3). These fine particles which were classified less than 150 μm were heated to oxidize their components in a muffle furnace at 90 K/h up to 1133 K and were maintained for 2 h on the roasting process.

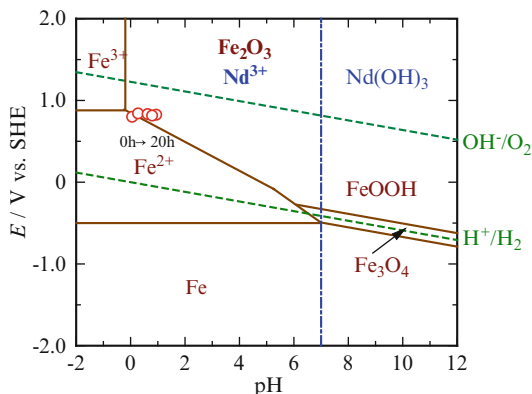
6.7.2 Wet Separation Process

The wet separation process was constituted of the leaching, deionization, and M (TFSA)_n amide salts synthesis. For the leaching process, the fine particles of the oxidized VCM were immersed in 1.0 mol dm⁻³ 1,1,1-trifluoro-*N*-[(trifluoromethyl) sulfonyl]methanesulfonamide (HN(SO₂CF₃)₂, HTFSA, Kanto Kagaku, >99.0 %) aqueous solution at 343 K for >12 h. The leaching reactions of RE and Fe components were expressed as follows:



In comparison with Nd–Fe–B magnet without roasting process, the leaching ratio of RE and Fe components in HTFSA solution increased and decreased, respectively. Considering from the total leaching quantity, 93.6 wt% of Nd and 18.1 wt% of Fe in Nd–Fe–B magnet components were found to be dissolved by one batch treatment. Thus, the leaching of Fe was prevented due to the formation of $\alpha\text{-Fe}_2\text{O}_3$ (hematite) layer on the roasting process. This leaching behavior was explained from the potential (*E*)-pH diagram of Fe–H₂O and Nd–H₂O systems as shown in Fig. 6.28, which showed the red circle determined from pH and ORP measurement of the actual leaching solution with different leaching times from 0 to 20 h. According to the *E*-pH diagram, under the condition of pH ~ 0.0 and *E* ~ 1.0, the most stable states of Fe and Nd are found to be $\alpha\text{-Fe}_2\text{O}_3$ (hematite) and Nd³⁺.

Fig. 6.28 *E*-pH diagram of Nd-H₂O (chain line) and Fe-H₂O (dotted line) systems



Therefore, the selective leaching of RE components proceeded in this condition. In the case of mineral acid, more than 99 % of RE components were leached, while the leaching of Fe was less than 0.5 %. On the contrary, more than 50 % of Fe was leached without roasting in mineral acid [51]. Then, Fe was selectively removed from HTFSA solution by the precipitation method after the oxidation treatment from Fe²⁺ to Fe³⁺ by O₂ bubbling. For the precipitation method, NaOH or KOH solution was applied as a kind of precipitant. The final precipitation formation of α -FeOOH was performed on the appropriate condition of pH \sim 4.5. The selective separation of α -FeOOH was explained from HSAB rule [52] and the related solubility products [53–56]. After the complete elimination of the precipitated α -FeOOH by centrifugation at 9840 G for 10 min (Model3740 Kubota Corp.), the HTFSA component including RE and alkali metal was evaporated in a draft chamber at 423 K. The obtained M(TFSA)_n salts with fine powder were dried in a chamber under vacuum at 393 K for 24 h. The component of each metal in the M(TFSA)_n salts was analyzed by ICP-AES analysis. Some compositions of the M(TFSA)_n salts were tabulated in Table 6.6.

6.7.3 Electrodeposition Process

After the wet separation process, the obtained M(TFSA)_n amide salts were dissolved in [P₂₂₂₅][TFSA] on the electrodeposition process. In the case of the three electrode systems as shown in Fig. 6.29, Cu cylindrical cathode was used for the electrodeposition. A prismatic Nd–Fe–B rod was employed as an anode and surrounded by a soda lime tube with a Vycor glass filter at the bottom in order to prevent the diffusion of dissolution components from the anode into the electrolyte. Then, Pt wire was applied as a quasi-reference electrode (QRE), because the

Table 6.6 Composition (wt %) of $M(\text{TFSA})_n$ amide salts with different conditions

| No. | Pr | Nd | Dy | Fe | Na | K | B | Trace metals | M (TFSA) _n | n |
|------------------|-------|-------|-------|-------------------|-------------------|-------|------|-------------------|-----------------------|------|
| 1-1 ^a | 13.40 | 38.86 | 10.73 | N.D. ^e | 5.23 | 30.23 | 1.55 | N.D. ^e | 547.87 | 1.73 |
| 1-2 ^a | 13.60 | 38.14 | 10.73 | N.D. ^e | 5.39 | 30.67 | 1.47 | N.D. ^e | 542.69 | 1.71 |
| 1-3 ^a | 11.20 | 32.99 | 9.38 | N.D. ^e | 6.03 | 37.83 | 1.35 | 1.23 | 484.51 | 1.53 |
| 2-1 ^b | 10.80 | 30.47 | 7.51 | N.D. ^e | 2.10 | 48.06 | 1.07 | N.D. ^e | 475.46 | 1.49 |
| 2-2 ^b | 11.04 | 30.10 | 7.56 | N.D. ^e | 2.16 | 48.10 | 1.04 | N.D. ^e | 474.48 | 1.49 |
| 3-1 ^c | 8.83 | 23.22 | 6.55 | N.D. ^e | 2.40 | 57.30 | 1.01 | 0.70 | 429.81 | 1.35 |
| 3-2 ^c | 9.52 | 20.77 | 6.89 | N.D. ^e | 2.52 | 59.50 | 1.02 | 0.71 | 421.97 | 1.33 |
| 3-3 ^c | 9.32 | 22.19 | 6.78 | N.D. ^e | 2.54 | 57.45 | 0.99 | 0.72 | 428.02 | 1.35 |
| 4-1 ^d | 19.84 | 49.90 | 1.65 | N.D. ^e | N.D. ^e | 26.20 | 1.94 | 0.47 | 627.38 | 1.98 |
| 4-2 ^d | 18.15 | 51.12 | 2.32 | N.D. ^e | N.D. ^e | 26.21 | 1.54 | 0.67 | 617.84 | 1.94 |

^aThe precipitant of NaOH and KOH in molar ratio of NaOH:KOH = 40:60

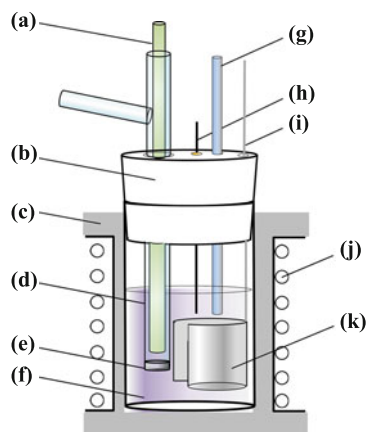
^bThe precipitant of NaOH and KOH in molar ratio of NaOH:KOH = 25:75

^cThe precipitant of NaOH and KOH in molar ratio of NaOH:KOH = 20:80

^dThe precipitant of NaOH and KOH in molar ratio of NaOH:KOH = 0:100

^eN.D. = not detected

Fig. 6.29 The schematic illustration of the electrodeposition cell, (a) Nd–Fe–B rod (anode), (b) silicon cap, (c) heat insulator, (d) soda lime glass tube, (e) Vycor glass filter, (f) $[\text{P}_{2225}][\text{TFSA}]$ including $M(\text{TFSA})_n$ amide salts, (g) K-type thermocouple, (h) Pt wire (QRE), (i) Cu wire, (j) mantle heater, and (k) Cu substrate (cathode)



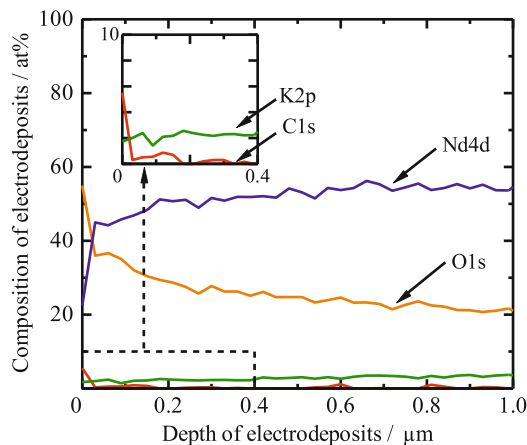


Fig. 6.30 The depth profile for each composition of the electrodeposits, —: C1s, —: O1s, —: Nd4d, —: K2p

potential of QRE was stabilized at elevated temperature. The electrodeposition was carried out at 373 K and the overpotential was controlled at -3.25 V vs. Pt QRE. After the electrodeposition, the electrodeposits were rinsed with a super dehydrated ethanol (Wako Pure Chemical Industries, Ltd., >99.5 %, the water content <50 ppm) in order to thoroughly remove the electrolyte adhered. The cathodic current density was estimated to be -0.18 mA cm $^{-2}$ during electrodeposition, and the current density decreased gradually with electrodeposition time due to the limitation of the diffusion controlled. The cathodic and anodic current efficiencies were found to be 84.7 % and 92.3 %, respectively. These efficiencies were reasonably good in this electrodeposition, because the cathodic and the anodic reactions proceeded smoothly during electrodeposition.

After the electrodeposition process, some blackish electrodeposits were obtained on Cu substrate. The surface morphology of the electrodeposits was the different sizes of fine particle structures with some particles from SEM observations. Nd components were detected from EDX spectrum. In order to analyze chemical state of the electrodeposits, the energy spectra were measured before and after sputtering for 50 min on XPS analysis. The depth profile for each composition of the black electrodeposits is represented in Fig. 6.30. It was confirmed that Nd metal existing in electrodeposits eliminated the top surface and the oxygen content in the electrodeposits was gradually decreased with the increase of the depth of electrodeposits. This result revealed that a large amount of Nd metal was detected in the middle layer of electrodeposits and the oxygen content was also decreased with the increase of the depth. Moreover, it was confirmed that the content of K in the electrodeposit was less than 2.0 at.%. Although the practical Nd–Fe–B magnet rod

was used as an anode substrate, Fe was not detected in the electrodeposits. This result indicates that the Vycor glass filter can be prevented from the diffusion of the dissolution components such as Fe. In addition, the Nd $3d_{5/2}$ spectrum in the surface of the electrodeposits was detected at 982.0 eV. On the other hand, the Nd $3d_{5/2}$ spectrum in the middle layer of the electrodeposits after sputtering treatment was assigned at 981.2 eV. Each Nd metal and oxide has the binding energy of Nd $3d_{5/2}$ at 980.5–981.0 eV and 981.7–982.3 eV, respectively, in the case of monochromated Al $K\alpha$ line [50]. According to the binding energy of Nd $3d_{5/2}$, the metallic state of Nd was ascertained on the middle layer of the electrodeposits, and the oxidation state of Nd appeared on the top surface of the electrodeposits.

6.7.4 Material Flow of Recovery Process

As described above, it is worthwhile for practical use to evaluate the material flow from all recovery processes such as pretreatment, wet separation, and electrodeposition using ILs. The material flow for all of recovery processes was displayed in Fig. 6.31, and the recovery target on this material flow was based on the oxidized Nd–Fe–B magnet wastes after roasting process.

As a first step of wet separation process, the selective leaching of RE components (93.5 % Nd and 66.7 % Dy) was performed on the leaching process. Then, the deironization treatment was executed by the precipitation method using the metallic hydroxide, and the residual Fe component was entirely removed on this process. After the iron removal treatment, the $M(\text{TFSA})_n$ amide salts were obtained from the synthesis process, and the yield of RE components was achieved more than 90 % on this process. Thus, a series of wet separation process enabled us to reveal that the 86.1 % Nd and 66.7 % Dy can be recovered as a $M(\text{TFSA})_n$ amide salt from the initial oxidized Nd–Fe–B magnet wastes. After the wet separation process, the $[\text{P}_{2225}][\text{TFSA}]$ including $M(\text{TFSA})_n$ amide salts was available as an electrolytic bath on the electrodeposition process. As for the calculation of material flow, the induced potential, $E = -3.25$ V; the current density, $I_d = -0.18$ mA cm^{-2} ; and the current efficiency, $\epsilon = 84.7$ %, were determined from the actual electrodeposition results described above. Assuming that total transported charge, $Q = 2960$ C, on a proper condition based on scaling up of the bath, the amount of 1.25 g Nd metal was recovered from this electrodeposition process, and the recovery yield calculated from the starting material (2.01 g Nd) was estimated to be 62.2 %. Therefore, this recovery process based on wet separation and electrodeposition processes using $M(\text{TFSA})_n$ amide salts and $[\text{P}_{2225}][\text{TFSA}]$ was valid for the practical Nd–Fe–B magnet wastes. Further improvement of the recovery process for RE metals is now in progress.

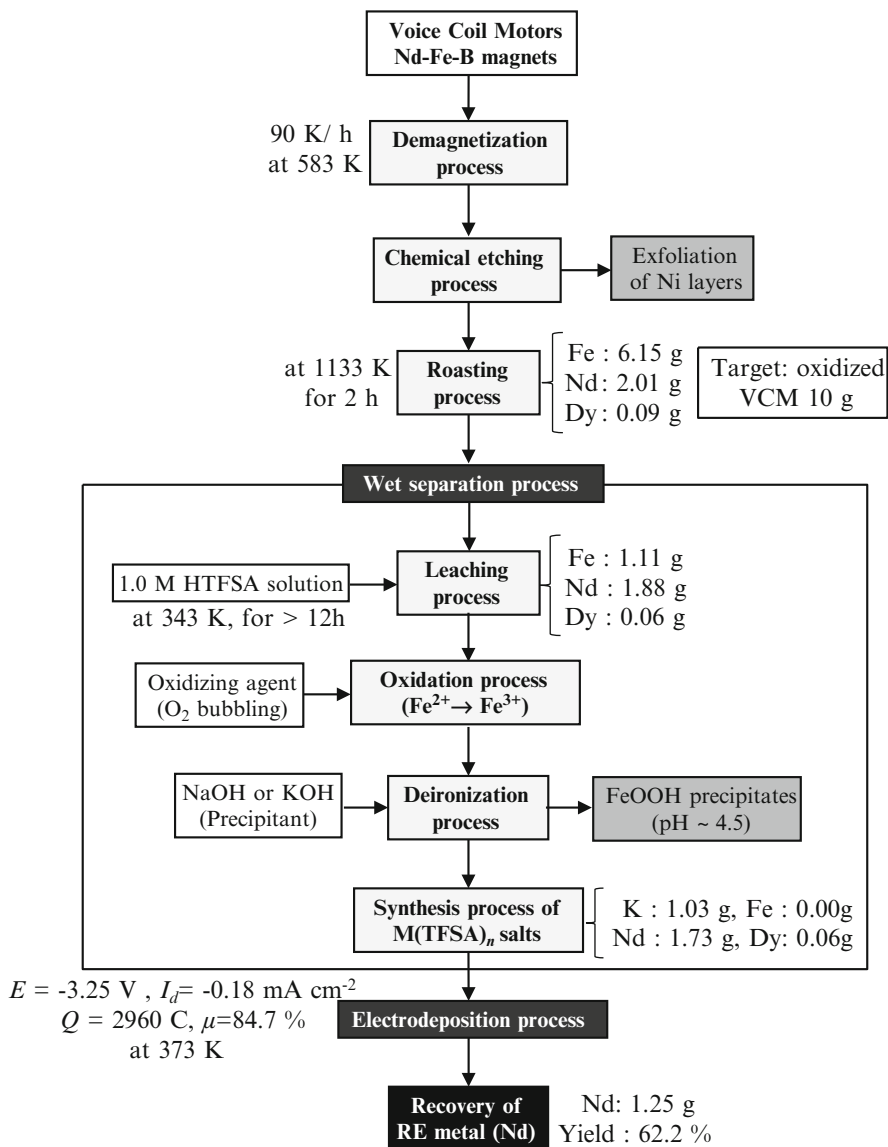


Fig. 6.31 Material flow of recovery process cooperated wet separation with electrodeposition using $M(\text{TFSA})_n$ salts and $[\text{P}_{2225}][\text{TFSA}]$

Acknowledgments This research was supported by the Environment Research and Technology Development Fund (3K123018) of the Ministry of the Environment, Japan. This work was partially supported by the Grant-in-Aid for Scientific Research (No. 15H02848) from the Ministry of Education, Culture, Sports, Science and Technology, Japan.

References

1. Yang J, Li X, Lang J, Yang L, Wei M, Gao M, Liu X, Zhai H, Wang R, Liu Y, Cao J (2011) Structural, optical and magnetic properties of Eu-doped ZnO films. *Mater Sci Semicond Process* 14:247–252
2. Rao RP, Devine DJ (2000) RE-activated lanthanide phosphate phosphors for PDP applications. *J Lumin* 87–89:1260–1263
3. Thiel CW, Böttger T, Cone RL (2011) Rare-earth-doped materials for applications in quantum information storage and signal processing. *J Lumin* 131:353–361
4. Yuan D, Liu Y (2006) Electrochemical preparation La–Co magnetic alloy films from dimethylsulfoxide. *Mater Chem Phys* 96:79–83
5. Du X, Graedel TE (2011) Global in-use stocks of the rare Earth elements: a first estimate. *Environ Sci Technol* 45:4096–4101
6. Matsuura Y (2006) Recent development of Nd–Fe–B sintered magnets and their applications. *J Magn Magn Mater* 303:344–347
7. Kobayashi S, Kobayashi K, Nohira T, Hagiwara R, Oishi T, Konishi H (2011) Electrochemical formation of Nd–Ni alloys in molten LiF–CaF₂–NdF₃. *J Electrochem Soc* 158:E142–E146
8. Uda T (2002) Recovery of rare earths from magnet sludge by FeCl₂. *Mater Trans* 43(1):55–62
9. Takeda O, Okabe TH, Umetsu Y (2006) Recovery of neodymium from a mixture of magnet scrap and other scrap. *J Alloys Compd* 408–412:387–390
10. MacFarlane DR, Forsyth M, Howlett PC, Pringle JM, Sun J, Annat G, Neil W, Izgorodina EI (2007) Ionic liquids in electrochemical devices and processes: managing interfacial electrochemistry. *Acc Chem Res* 40:1165–1173
11. Simka W, Puszczuk D, Nawrat G (2009) Electrodeposition of metals from non-aqueous solutions. *Electrochim Acta* 54:5307–5319
12. Legeai S, Diliberto S, Stein N, Boulanger C, Estager J, Papaiconomou N, Draye M (2008) Room-temperature ionic liquid for lanthanum electrodeposition. *Electrochem Commun* 10:1661–1664
13. Bhatt AI, May I, Volkovich VA, Collison D, Helliwell M, Polovov IB, Lewin RG (2005) Structural characterization of a lanthanum bistriflimide complex, La(N(SO₂CF₃)₂)₃(H₂O)₃, and an investigation of La, Sm, and Eu electrochemistry in a room-temperature ionic liquid, [Me₃NnBu][N(SO₂CF₃)₂]. *Inorg Chem* 44:4934–4940
14. Londermeyer J, Multerer M, Zistler M, Jordan S, Gores HJ, Kipferl W, Dia-conu E, Sperl M, Bayreuther G (2006) Electroplating of dysprosium, electrochemical investigations, and study of magnetic properties. *J Electrochem Soc* 153(4):C242–C248
15. Ishii M, Matsumiya M, Kawakami S (2012) Development of recycling process for rare earth magnets by electrodeposition using ionic liquids media. *ECS Trans* 50(11):549–560
16. Kondo H, Matsumiya M, Tsunashima K, Kodama S (2012) Attempts to the electrodeposition of Nd from ionic liquids at elevated temperatures. *Electrochim Acta* 66:313–319
17. Kondo H, Matsumiya M, Tsunashima K, Kodama S (2012) Investigation of oxidation state of the electrodeposited neodymium metal related with the water contents of phosphonium ionic liquids. *ECS Trans* 50(11):529–538
18. Tsuda N, Matsumiya M, Tsunashima K, Kodama S (2012) Electrochemical behavior and solvation analysis of rare earth complexes in ionic liquids media investigated by SECM and Raman spectroscopy. *ECS Trans* 50(11):539–548
19. Matsumiya M, Ishii M, Kazama R, Kawakami S (2014) Electrochemical analyses of diffusion behaviors and nucleation mechanisms for neodymium complexes in [DEME][TfSA] ionic liquid. *Electrochim Acta* 146:371–377
20. Kurachi A, Matsumiya M, Tsunashima K, Kodama S (2012) Electrochemical behavior and electrodeposition of dysprosium in ionic liquids based on phosphonium cations. *J Appl Electrochem* 42:961–968

21. Kazama R, Matsumiya M, Tsuda N, Tsunashima K (2013) Electrochemical analysis of diffusion behavior and nucleation mechanism for Dy(II) and Dy(III) in phosphonium-based ionic liquids. *Electrochim Acta* 113:269–279
22. Apelblat A, Manzurola E (1999) Solubilities of *o*-acetylsalicylic, 4-aminosalicylic, 3,5-dinitrosalicylic, and *p*-toluic acid, and magnesium–aspartate in water from $T = (278 \text{ to } 348) \text{ K}$. *J Chem Thermodyn* 31:85–91
23. Ren Y, Shui H, Peng C, Liu H, Hu Y (2011) Solubility of elemental sulfur in pure organic solvents and organic solvent–ionic liquid mixtures from 293.15 to 353.15 K. *Fluid Phase Equilib* 312:31–36
24. Peter K (1993) Free energy calculations: applications to chemical and biochemical phenomena. *Chem Rev* 93:2395–2417
25. Gu W, Rahi SJ, Heim V (2004) Solvation free energies and transfer free energies for amino acids from hydrophobic solution to water solution from a very simple residue model. *J Phys Chem B* 108:5806–5814
26. Rey I, Johansson P, Lindgren J, Lassegues JC, Grondin J, Servant L (1998) Spectroscopic and theoretical study of $(\text{CF}_3\text{SO}_2)_2\text{N}^-$ (TFSI⁻) and $(\text{CF}_3\text{SO}_2)_2\text{NH}$ (HTFSI). *J Phys Chem A* 102:3249–3258
27. Edman L (2000) Ion association and ion solvation effects at the crystalline–amorphous phase transition in PEO – LiTFSI. *J Phys Chem B* 104:7246–7254
28. Umebayashi Y, Mitsugi T, Fukuda S, Fujimori T, Fujii K, Kanzaki R, Takeuchi M, Ishiguro S (2007) Lithium ion solvation in room-temperature ionic liquids involving bis(trifluoromethanesulfonyl) imide anion studied by raman spectroscopy and DFT calculations. *J Phys Chem B* 111:13028–13032
29. Carnall WT, Fields PR, Rajnak K (1968) Electronic energy levels in the trivalent lanthanide aquo ions. I. Pr^{3+} , Nd^{3+} , Pm^{3+} , Sm^{3+} , Dy^{3+} , Ho^{3+} , Er^{3+} , and Tm^{3+} . *J Chem Phys* 49:4424–4442
30. Chambers MD, Clarke DR (2009) Doped oxides for high-temperature luminescence and lifetime thermometry. *Annu Rev Mater Res* 39:325–359
31. Su Q, Pei Z, Chi L, Zhang H, Zhang Z, Zou F (1993) The yellow-to-blue intensity ratio (Y/B) of Dy^{3+} emission. *J Alloys Compd* 192:25–27
32. Pei Z, Su Q, Li S (1991) Investigation on the luminescence properties of Dy^{3+} and Eu^{3+} in alkaline-earth borates. *J Lumin* 50:123–126
33. Katase T, Imashuku S, Murase K, Hirato T, Awakura Y (2006) Water content and related physical properties of aliphatic quaternary ammonium imide-type ionic liquid containing metal ions. *Sci Technol Adv Mater* 7:502–510
34. Yoshizawa M, Xu W, Angell CA (2003) Ionic liquids by proton transfer: vapor pressure, conductivity, and the relevance of ΔpK_a from aqueous solutions. *J Am Chem Soc* 125:15411–15419
35. Goto M, Oldham KB (1973) Semiintegral electroanalysis. Shapes of neopolarograms. *Anal Chem* 45(12):2043–2050
36. Mahon PJ, Oldham KB (1998) Voltammetric modelling via extended semi-integrals. *J Electroanal Chem* 445:179–195
37. Matsuda H, Ayabe Y (1955) Zurtheorie der randles-sev.ickschenkathodenstrahl- polarographie. *Z Elektrochem* 59:494–503
38. Dalrymple-alford P, Goto M, Oldham KB (1977) Shapes of derivative neopolarograms. *J Electroanal Chem* 85:1–15
39. Scharifker B, Hills G (1983) Theoretical and experimental studies of multiple nucleation. *Electrochim Acta* 28:879–889
40. Bando Y, Katayama Y, Miura T (2007) Electrodeposition of palladium in a hydrophobic 1-*n*-butyl-1-methylpyrrolidinium bis(trifluoromethylsulfonyl)imide room-temperature ionic liquid. *Electrochim Acta* 53:87–91
41. Tachikawa N, Serizawa N, Katayama Y, Miura T (2008) Electrochemistry of Sn(II)/Sn in a hydrophobic room-temperature ionic liquid. *Electrochim Acta* 53:6530–6534

42. Zhu Y-L, Kozuma Y, Katayama Y, Miura T (2009) Electrochemical behavior of Ni(II)/Ni in a hydrophobic amide-type room-temperature ionic liquid. *Electrochim Acta* 54:7502–7506
43. Basile A, Bhatt AI, O'Mullane AP, Bhargava SK (2011) An investigation of silver electrodeposition from ionic liquids: influence of atmospheric water uptake on the silver electrodeposition mechanism and film morphology. *Electrochim Acta* 56:2895–2905
44. Fukui R, Katayama Y, Miura T (2011) The influence of potential on electrodeposition of silver and formation of silver nanoparticles in some ionic liquids. *J Electrochem Soc* 158(9):D567–D572
45. Mostany J, Mozota J, Scharifker BR (1984) Three-dimensional nucleation with diffusion controlled growth: Part II. The nucleation of lead on vitreous carbon. *J Electroanal Chem* 177:25–37
46. Gunawardena GA, Hills GJ, Montenegro I (1978) Potentiostatic studies of electrochemical nucleation. *Electrochim Acta* 23:693–697
47. Yang M-H, Sun I-W (2003) Electrodeposition of antimony in a water-stable 1-ethyl-3-methylimidazolium chloride tetrafluoroborate room temperature ionic liquid. *J Appl Electrochem* 33:1077–1084
48. Grujicic D, Pesic B (2005) Reaction and nucleation mechanisms of copper electrodeposition from ammoniacal solutions on vitreous carbon. *Electrochim Acta* 50:4426–4443
49. Matsumiya M, Kamo Y, Hata K, Tsunashima K (2013) Solvation structure of iron group metal ion in TFSA-based ionic liquids investigated by raman spectroscopy and DFT calculations. *J Mol Struct* 1048:59–63
50. Moulder JF, Stickle WF, Sobol PE, Bomben KD (1992) Handbook of X-ray photo-electron spectroscopy. Perkin-Elmer Corp., Eden Prairie
51. Tanaka M, Oki T, Koyama K, Narita H, Oishi T (2013) Recycling of rare earths from scrap. *Handb Phys Chem Rare Earths* 43:159–212
52. Pearson RG (1988) Absolute electronegativity and hardness: application to inorganic chemistry. *Inorg Chem* 27:734–740
53. Diakonov II, Ragnarsdottir KV, Tagirov BR (1998) Standard thermodynamic properties and heat capacity equations of rare earth hydroxides: – II. Ce(III)-, Pr-, Sm-, Eu(III)-, Gd-, Tb-, Dy-, Ho-, Er-, Tm-, Yb-, and Y-hydroxides. Comparison of thermochemical and solubility data. *Chem Geol* 151:327–347
54. Gnanaprakash G, Philip J RB (2007) Effect of divalent metal hydroxide solubility product on the size of ferrite nanoparticles. *Mater Lett* 61:4545–4548
55. Michelle M, Joseph M, Renee F (2008) Determining the solubility product of Fe(OH)₃: an equilibrium study with environmental significance. *J Chem Educ* 85(2):254–255
56. Diakonov I, Khodakovskiy I, Schott J, Sergeeva E (1994) Thermodynamic properties of iron oxides and hydroxides. I. Surface and bulk thermodynamic properties of goethite (α -FeOOH) up to 500 K. *Eur J Mineral* 6:967–983